2011

Calibration of a fieldable imaging pyrometer for use with hydrocarbon flames

Jonathan Braun Hanks

CALIBRATION OF A FIELDABLE IMAGING PYROMETER FOR USE WITH HYDROCARBON FLAMES

by

JONATHAN BRAUN HANKS

A THESIS

Submitted in partial fulfillment of the requirements
for the degree of Master of Science in Engineering
in
The Department of Electrical and Computer Engineering
to
The School of Graduate Studies
of
The University of Alabama in Huntsville

HUNTSVILLE, ALABAMA
2011

In presenting this thesis in partial fulfillment of the requirements for a masters degree from The University of Alabama in Huntsville, I agree that the Library of this University shall make it freely available for inspection. I further agree that permission for extensive copying for scholarly purposes may be granted by my advisor or, in his/her absence, by the Chair of the Department or the Dean of the School of Graduate Studies. It is also understood that due recognition shall be given to me and to The University of Alabama in Huntsville in any scholarly use which may be made of any material in this thesis.

Jonathan Braun Hanks (Jonathan Braun Hanks)

March 15th, 2011 (March 15th, 2011)

THESIS APPROVAL FORM

Submitted by Jonathan Braun Hanks in partial fulfillment of the requirements for the degree of Master of Science in Engineering and accepted on behalf of the Faculty of the School of Graduate Studies by the thesis committee.

We, the undersigned members of the Graduate Faculty of The University of Alabama in Huntsville, certify that we have advised and/or supervised the candidate on the work described in this thesis. We further certify that we have reviewed the thesis manuscript and approve it in partial fulfillment of the requirements for the degree of Master of Science in Engineering.

3/11/11 Committee Chair
John D. Williams (Date)

03/08/11
Shankar Mahalingam

3/10/11
Reza Adhami

3/10/11 Department Chair
Robert Lindquist

03/08/11 College Dean
Shankar Mahalingam

5/9/11 Graduate Dean
Rhonda K. Gaede

ABSTRACT

The School of Graduate Studies
The University of Alabama in Huntsville

Degree Master of Science College/Dept. Engineering / Electrical and Computer Engineering

Name of Candidate Jonathan Braun Hanks

Title Calibration of a Fieldable Imaging Pyrometer for use with Hydrocarbon Flames

There is a growing need in both the industrial and academic communities to further the understanding of hydrocarbon flame combustion. As such, there is high demand for fieldable scientific research tools to expand the current knowledge base. This research paper presents a novel method for the design and calibration of an imaging pyrometry sensor for use in measuring the temperature distribution of hydrocarbon flames. Unlike other laboratory based setups, the described sensor is both passive and self contained. This thesis aims to describe the proposed technology, calibration procedure, and data reduction algorithms, using field tested results.

Abstract Approval: Committee Chair — John D. Williams

Department Chair — Robert Lindquist 3/10/11

Graduate Dean — Ronda K. Gaede 5/9/11

ACKNOWLEDGMENTS

.

For my wife Jamie, my parents Louis and Elizabeth, my friends, my family, and my puppy Minnie for keeping me company while I worked. I love you all and thank you for your support. I give special thanks to Polaris Sensor Technologies, Inc. and the USAF 46th Test Wing for their support of this work.

TABLE OF CONTENTS

Page

LIST OF FIGURES

Figure **Page**

LIST OF TABLES

Table **Page**

LIST OF EQUATIONS

CHAPTER 1

INTRODUCTION TO FLAME PYROMETRY

1.1. Hydrocarbon Flames

For over 100 hundred years, hydrocarbon fuels have served as the backbone of the industrial world. With an inherently combustible nature, there are practical concerns regarding the safe storage, transportation, and delivery of these fuels. As such, there is a significant call for innovative sensor technology that is capable of reporting both the existence and location of a flame event with a high degree of accuracy. Such a sensor would have commercial, industrial, and military applications [**1**,**2**,**3**,**4**,**5**]. This need drives scientific research to further the understanding of burn profiles in hydrocarbon flames. The primary impetus for this research paper is to develop an intelligent sensor capable of monitoring an area of interest while autonomously reporting when a flame event occurs.

For the purposes of this paper, carbon sooting flames are chosen as the area of interest because they cover such a wide range of potential fuel sources: both natural and man-made [**6**]. For hydrocarbon flames, the primary radiator is the carbon soot particle released by the combustion process [**7**]. Because carbon soot is common among all hydrocarbon flames, a pyrometry sensor based on the detection of these particles will deliver the most versatile flame detection capability.

Several methods exist for flame detection including thermocouples, chemical analyzers, and optical detection. However, given the nature of a fire, there exists the potential for flame detection hardware to become damaged by heat. With this in mind,

the cost effectiveness of these approaches must be evaluated in order to select the best detection scheme. To mitigate the risk presented to the sensor, the most straightforward solution is to employee a sensor that can operate at a significant standoff distance from the fire. Thermocouples and chemical analyzers are not well suited to operate at standoff distances because they are designed to analyze their immediate environment. The author believes that an optics based approach is the best solution for the problem at hand [**8**].

In past decades, optical detector technology and computing power have both advanced to become well suited for real-time standoff detection of flame events. The main categories of modern optical detectors are single-element monolithic detectors and pixilated detector arrays. These are commonly referred to as non-imaging and imaging detection architectures. While non-imaging detectors offer many advantages, this paper will focus on an imaging detection architecture. Imaging detectors are capable of providing enhanced geometric situational awareness, which is critical for monitoring fires over a large area.

Imaging detection schemes can be further broken down into two subcategories. The first is an image processing based approach where the flame is identified within the scene by using some metric to distinguish it from the background [**9**]. There are numerous approaches to identify flame images, with the most common being edge detection via some statistical metric and intensity thresholding [**10**,**11**]. Additional techniques exist that seek to exploit a fire's transient properties, specifically flame flicker, in order to report the flame's location [**12**].

In addition to purely image-based processing techniques, there also are radiometric techniques. Here, the underlying goal is obtain information about the nature of the radiation emitted by the flame. Specifically, the most common form of optical

characterization is to measure the flame spectral emission. Many have accomplished this by employing color cameras to define the color space occupied by a flame [**13**,**14**,**15**]. By contrast this paper proposes a novel method to calculate a flames temperature based on its color space. From this temperature calculation, the sensor is then able to separate the flame from the rest of the scene with a high degree of accuracy. The key to accomplishing this task is to understand the flame's spectral emissions. This makes it possible to identify specific spectral characteristics that are unique to flame sources. Fire detection and identification is then achieved by distinguishing between flame and non-flame portions of the scene based on this temperature analysis.

Both image processing and radiometric techniques offer certain advantages and disadvantages for flame detection. Therefore, it is reasonable to conclude that both these approaches should be utilized in order to develop a robust flame detection system.

Scientific grade imaging detectors are available in a wide range of formats and cover wavebands from UV to long wave infrared. Given the variety of detection schemes, there are several steps necessary to select the optimal sensor format. As a starting point, research must be done to understand the emission profile of carbon soot [**16**,**17**,**18**]. This information can be obtained through both literature surveys and laboratory measurements. Once the flame emission spectrum is understood, it will be possible to identify the best detection waveband and sensor architecture. The chosen sensor can then be characterized and its performance evaluated. From this evaluation, it will be possible to develop both calibration and data reduction algorithms to allow the sensor to perform as an imaging pyrometer. Furthermore, image processing techniques can further aid in the identification of flame events and these methods should be

explored. As a final verification of the pyrometry sensor's performance should be conducted using representative hydrocarbon flames with known characteristics.

This research paper implements these prescribed steps in order to develop a fieldable imaging pyrometer for use with hydrocarbon flames. The author presents an argument for a novel method for calibrating an imaging pyrometry sensor for use in measuring the spatial temperature distribution of hydrocarbon flames. The goal of this effort will be to design a sensor that is completely passive and self contained. The approach described will make no assumptions as to the value of the flame's emissivity other than the flame's emissivity can be approximate as constant across the visible waveband. This ability to account for emissivity is a crucial component for designing a fieldable sensor [**19**].

1.2. Flame Emission Spectrum Measurements

Several candidate technologies have the potential to be used as an imaging pyrometry sensor. These technologies included UV, visible, NIR, MWIR, and LWIR commercially available sensors and have been utilized in flame detection using various methods [**20**,**21**,**22**]. Because these sensor options cover such a wide spectral band, an initial experiment was devised to simultaneously measure the spectral output of a single flame across all possible wavebands. To accomplish this task, two spectrometers were integrated into a single setup.

Both spectrometers were used to collect the emission profile of a hydrocarbon flame. The first was a HR2000+ spectrometer from Ocean Optics used to measure across a wavelength range from 200 nm to 1100 nm (UV, Visible and NIR). The other spectrometer, a MIDAC FTIR, was used to measure from 2.5 μm to over 15 μm (MWIR

and LWIR). The FTIR and associated software were made available to Polaris Sensor Technologies, Inc. through a CRADA with UA Huntsville. This spectrometer pair covers a very wide waveband from 200 nm to 25 μm. There is a noticeable measurement gap between 1.1 μm and 2.5 μm. This missing waveband was not avoided for any particular reasons other than spectrometers that are sensitive to this spectral range are not as readily available or as cost effective.

To couple the light from the flame into the spectrometers, a custom breadboard was designed with two separate optical trains. This was necessary to match the required F/# and magnification requirements of each spectrometer. In order to insure the systems would perform properly, they were first modeled in the ZEMAX software suite. The optical system was designed with off the shelf optical components, which were then mounted on the custom breadboard. See **Figure 1.1**, below, for breadboard layout. The setup presented in this figure was designed in collaboration with John Harchanko and John Reinheardt of Polaris Sensor Technologies.

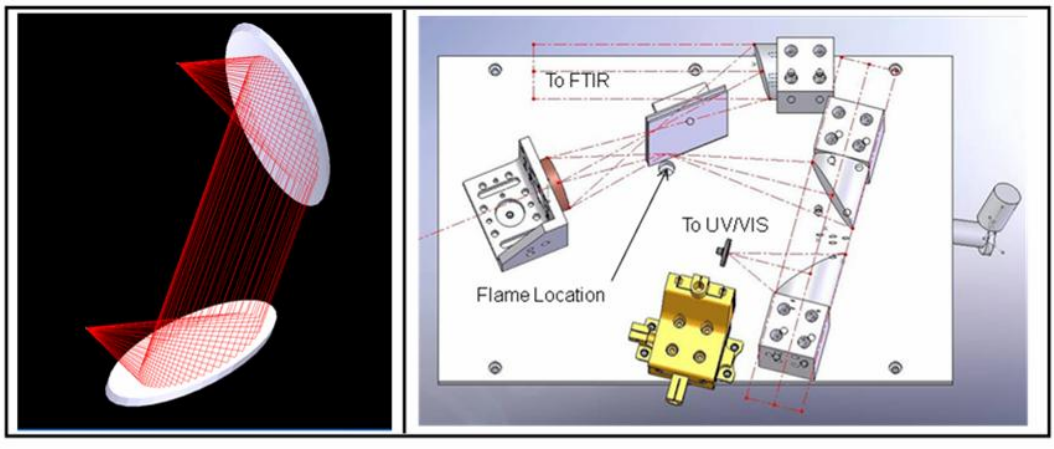

Figure 1.1 ZEMAX layout of UV/VIS collection mirrors (left), Solid Works™ layout of optical pyrometry breadboard setup (right).

The experimental setup is designed to use the two spectrometers to simultaneously analyze the emissions from a flame source to provide broadband spectral data. In order to ensure accurate measurements, a calibration lamp was used for the UV-Visible spectrometer (the HR2000+). This calibration allowed the UV-Visible spectrometer to act as a spectroradiometer. The dual spectrometer experiment measured different hydrocarbon fuels at various burn profiles to determine their spectral output. As such, this experimental design determined which waveband (UV, Vis or IR) was best suited for measuring flame temperature. In turn, the waveband comparison would guide the selection of an imaging sensor for flame pyrometry.

An example of data collected in the dual spectrometer experiment from an acetylene flame is shown below in **Figure 1.2**. The experiment showed that the spectral emission in the UV-to-NIR waveband corresponded very closely to a theoretical Black Body curve. In contrast, the MWIR and LWIR wavebands revealed high absorption bands near 2.5 microns (atmospheric H_20 and CO_2) and 4.5 microns (atmospheric CO_2) **[23]**. It is anticipated that these absorption bands will pose extreme difficulty if the envisioned sensor is to be used without any a priori knowledge of the distance to the flame. The visible portion of the spectrum showed no significant sign of absorption bands, indicating that at large standoff distances, the flame emission spectrum would still appear to behave as a blackbody radiator. However, there were noticeable spikes in the visible flame measurements **Figure 1.2 (left)**. It was believed that these spikes were due to a bend in fiber optic spectrometer, causing an error in the calibration. To confirm this hypothesis, additional flame measurements were taken with a fieldable spectrometer that required no fiber input calibration. A more detailed description of these measurements is

provided in the next section. This data was produced in collaboration with John Harchanko, Polaris Sensor Technologies.

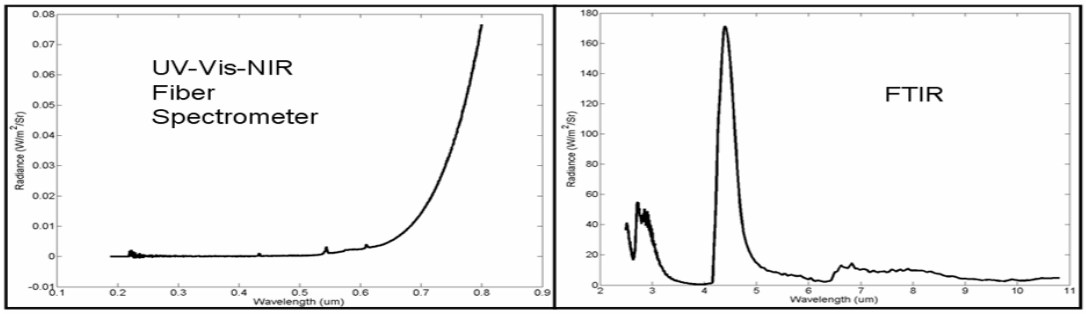

Figure 1.2 Acetylene flame spectral emission in both the UV-Visible (left) and IR (right) wavebands.

1.3. Validation of Visible Measurements

The emission spikes seen in the UV-Visible spectrum of **Figure 1.2** are believed to be artifacts of the spectrometer's calibration procedure. Calibration of the HR2000+ is achieved by recording responsivity measurements of the sensor using a known Deuterium-Halogen Source. This allows the sensor to achieve an absolute radiometric calibration. However, after calibration, the fiber must be removed from the calibration source and placed in the breadboard setup shown in **Figure 1.1**. Though care was taken to avoid extreme bends, the fiber necessarily had to be moved as it was placed in the setup. To confirm that hydrocarbon flames act as true blackbody radiators, additional measurements were taken in the lab using a SP-100, which is an NIST traceable spectroradiometer from ORB Optronix. An example of the data collected from an acetone pan fire using the SP-100 is presented in **Figure 1.3**.

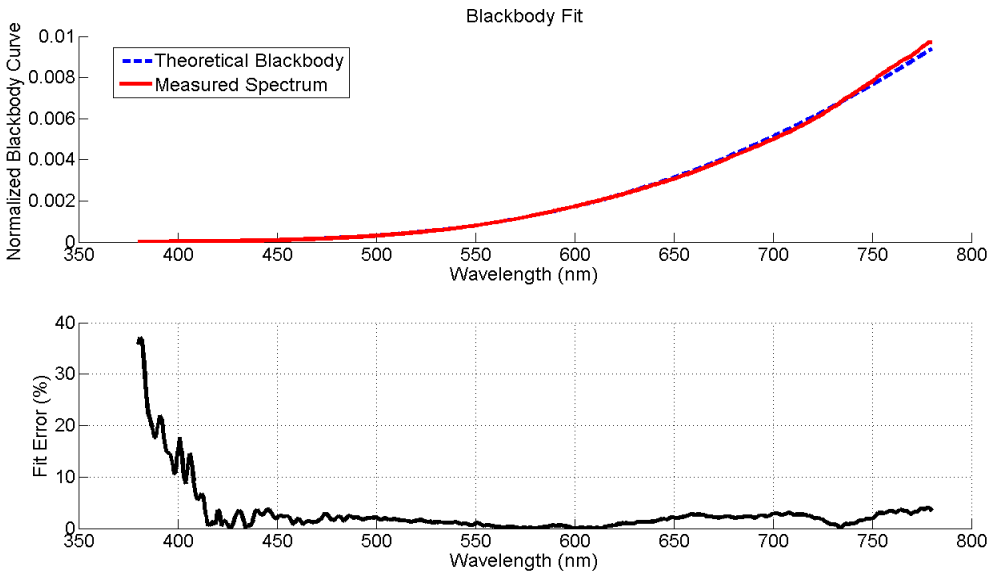

Figure 1.3 Spectral emission of acetone flame measured using SP-100 spectroradiometer (top) and the fit error between the spectral radiance and a theoretical blackbody curve. (bottom)

The SP-100 has no external fiber and thus does not share the same mounting sensitivity as the HR2000+. The SP-100 was used as a secondary spectroradiometer because it is only sensitive between 380 nm and 780 nm. This sensitivity range is sufficient for further analysis of the visible waveband, but the HR2000+ was required for the initial flame measurements because it could measure the UV and NIR as well as the visible wavelengths. This data validates the use of the blackbody radiator model in the visible waveband. This knowledge will be used as the basis for the design, calibration, and testing of a fieldable imaging pyrometer for use with hydrocarbon flames.

CHAPTER 2

SENSOR SELECTION AND DESIGN

2.1. Selection of Sensor Architecture

From the data analysis presented in the previous section, the visible region will be considered the desired waveband for the pyrometer sensor to operate. Furthermore, given the dynamic nature of a hydrocarbon flame, the proposed sensor must have sufficient temporal and special resolution to adequately resolve the flame's characteristics. To meet this requirement, a visible digital camera with an integrated silicon based Focal Plane Array (FPA) was chosen as the optimal architecture for the imaging flame pyrometer sensor. FPA's offer a unique advantage in that the data collected is spatially and temporally aligned by design. Silicon based visible cameras typically offer an order of magnitude lower cost compared to LWIR sensors and two orders of magnitude lower cost compared to MWIR sensors. Furthermore, unlike the numerous absorption bands seen in the spectrometer data, the spectral data in the visible region avoids the strong chemical absorption bands that must be considered when analyzing the flame's spectral emission profile in the infrared [**24**].

With the advent of modern CCD and CMOS FPA's, many pyrometers have been developed in recent years that utilize this technology. These sensors utilize an FPA based approach in order to achieve high spatial resolution but also require custom optics trains [**25**,**26**], or custom bandpass filters [**27**]. While effective, the use of custom optics inevitably drive up the sensor's cost due to expensive optical hardware. With the

inherent potential for hardware damage due to the destructive nature of flames, a low cost, FPA-based sensor solution is need. Fortunately, the cost of silicon based FPAs has decreased in recent years due to the demand for consumer grade digital cameras. It is anticipated that this technology will further improve with continued research [**28**]. Consequently, silicon FPA's with integrated red, green, and blue broadband color filters (commonly referred to as Bayer filters) are now an industry standard for scientific grade cameras with a variety of digital interfaces [**29**]. Therefore, an imaging pyrometer based on a color scientific camera with integrated Bayer filters and a COTS objective lens would address the need for a low cost sensor by avoiding the need for custom optics. By the exploiting FPA's integrated Bayer filters, there is no need for spatial and/or temporal image registration, thus avoiding a computationally intense processing step [**30**]. This is ideal as temporal registration is only suited for controlled laboratory burns [**31**]. The remainder of this paper will present a technique for calibrating such a sensor as well as the data reduction algorithms required to calculating flame temperature in the field.

2.2. The Multi-Color Pyrometry Method

As previously described, pyrometers that utilize the visible and NIR waveband have existed for several years. A standard approach, known as the multi-color method, is employed to calculate the temperature of a blackbody based on its spectral emission profile. This technique has proven to be one of the most common techniques employed by imaging pyrometers [**32**,**33**,**34**,**35**]. A brief description of this approach is provided in this section.

The underlying principle of this technique is that carbon soot particles operate as blackbody radiators, and thus the temperature of a flame can be determined using

Planck's Blackbody Law. Planck's equation for the spectral radiance emission of blackbody is given below in **Equation 2.1**, where wavelength (λ) is in units of microns, and temperature (T) is in Kelvin.

$$L_\lambda = \frac{\varepsilon_\lambda \cdot hc^2}{\lambda^5 \cdot \left(\exp\left(hc/k\lambda T\right) - 1\right)} \tag{2.1}$$

The Blackbody Law predicts that the spectral emission of a Blackbody radiator at a given wavelength is based on the surface temperature of the object. Given two specific wavelengths, **Equation 2.1** can be manipulated for each wavelength so that the temperature can be calculated directly, as shown below in **Equation 2.2** [**36**]. This is accomplished by incorporating the spectral emissivity equation which was derived by Hottel and Broughton, shown below in **Equation 2.3**, where k is the complex component of the index of refraction, ℓ is the optical path length, and α is an empirically determined constant whose unitless value is 1.39 for carbon soot in the visible waveband [**37**].

$$T = \left(\frac{hc}{k}\right) \cdot \left(\frac{1}{\lambda_2} - \frac{1}{\lambda_1}\right) \cdot \ln\left(\frac{\varepsilon_2 \cdot L_{\lambda_1} \cdot \lambda_1^{\,5}}{\varepsilon_1 \cdot L_{\lambda_2} \cdot \lambda_2^{\,5}}\right)^{-1} \tag{2.2}$$

$$\varepsilon_\lambda = 1 - \exp(-k \cdot \ell \cdot \lambda^{-\alpha}) \tag{2.3}$$

Strictly speaking, **Equation 2.3** indicates that the emissivity varies as a function of wavelength. However, for this discussion, carbon soot serves as the blackbody

radiator which has an inherently high *k* value in the UV-to-NIR waveband [**38**]. The result is that the flame can be assumed to have unit emissivity for portions of the flame with high soot production [**39**]. Therefore, as a matter of practicality, the emissivity of dense soot regions of a hydrocarbon flame can be approximate as having a value of 1 in the visible waveband. Furthermore, because the proposed sensor is designed to be a fieldable pyrometer, it can be assumed that there is a reasonable separation between the sensor and the flame, implying that only flames of significant size will be resolvable. Based on this assumption, as per **Equation 2.3**, unit flame emissivity will be considered because large flames by definition have large optical path lengths.

For the purposes of this paper, large path lengths will be considered to be any portion of the flame where soot formation is significant enough that the flame is not translucent. The assumption of high soot production is significant when considering that areas of low soot production have a resulting low emissivity [**40**]. A method for distinguishing portions of the flame with high soot production from translucent regions is discussed later on in **Section 6.2.3**.

As the Multi-Color method has been employed by several other groups, an analysis will be made to predict if this technique can be adapted for a color scientific camera using the broadband Bayer filters instead of narrow bandpass filters. While Bayer filters transmission profiles vary between manufacturers, they typically have peak wavelengths around 480nm, 540nm, and 620nm for the blue, green, and red filters respectively. For various temperatures, the ratios between narrow band filters (green divided by blue, and red divided by green) as predicted by **Equation 2.2** are given below in **Figure 2.1**.

The trend lines predicted by this simulation demonstrate that regardless which of the two color channels are used to calculate the spectral ratios, both trend lines follow a pseudo-linear progression. It must now be determined if the trend lines predicted by this simulation can be repeated using a silicon FPA with integrated Bayer filters. This will determine if the existing multi-color method is applicable when using the FPA's broadband Bayer filters.

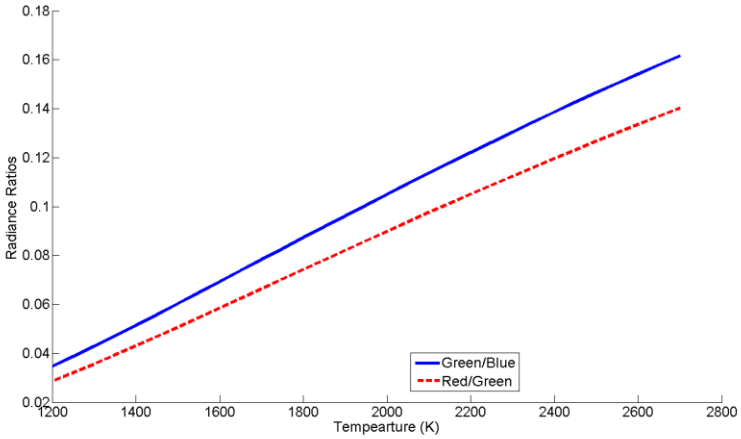

Figure 2.1 Theoretically predicted spectral ratios versus temperature.

2.3. Initial Sensor Observations

To evaluate the multi-color method using Bayer filters, a COTS color CMOS camera was calibrated using a laboratory blackbody source with measurements taken at several different temperatures. The sensor has integrated Bayer color filters with an 8-bit dynamic range. The average pixel counts for all three color channels are recorded at each temperature setting for the laboratory blackbody. The purpose of this experiment is to calculate the color ratios generated when the sensor views a laboratory blackbody source. The measured values will then be compared to the ratios to the simulation shown in **Figure 2.1**. Thus, **Equation 2.2** is exercised by taking the ratio between the count values

reported by any of the two color channels. The setup of this experiment is shown below in **Figure 2.2**.

The laboratory blackbody source is a Mikron M360 which is capable of producing a uniform temperature across the aperture to within 0.1% of the temperature reported by its integrated thermocouple. The blackbody has an advertised total temperature accuracy of 0.2% and an emissivity of .995 [**41**]. The imaging pyrometer is based on a DFK 21BUC03 color camera from The Imaging Source. The camera's CMOS FPA is 640 x 480 pixels and can achieve frame rates of up to 60 Hz. The power, camera interface, and digital image/video capture are achieved on the computer via a USB interface.

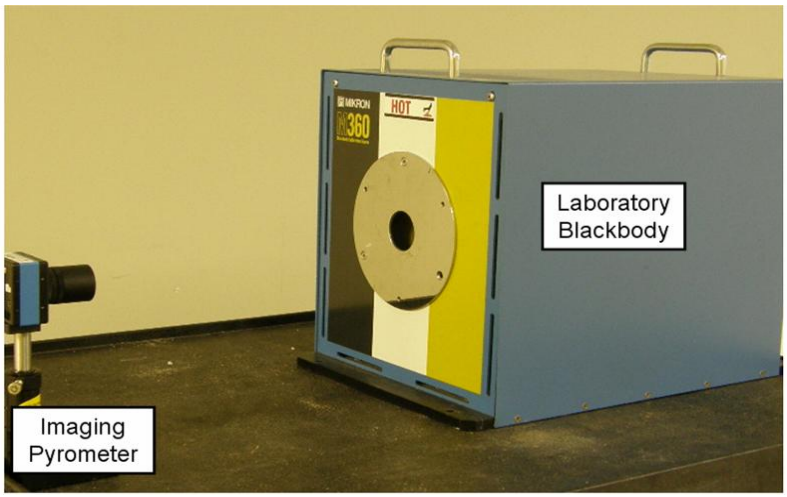

Figure 2.2 Calibration of the imaging pyrometer using a laboratory blackbody

As anticipated, trend lines of the data measured by the cameras will not exactly match those predicted by the simulation. The reason for this was that the spectral response of the camera is not flat. Thus, the slope of each trend line measured in the lab should differ from the model but only by a positive scalar. Initial blackbody measurements were taken at 1273, 1323 K, and 1373 K blackbody. The purpose of these

measurements was to evaluate the camera's sensitivity to changes in blackbody temperature. The results for this experiment are given below in **Figure 2.3**.

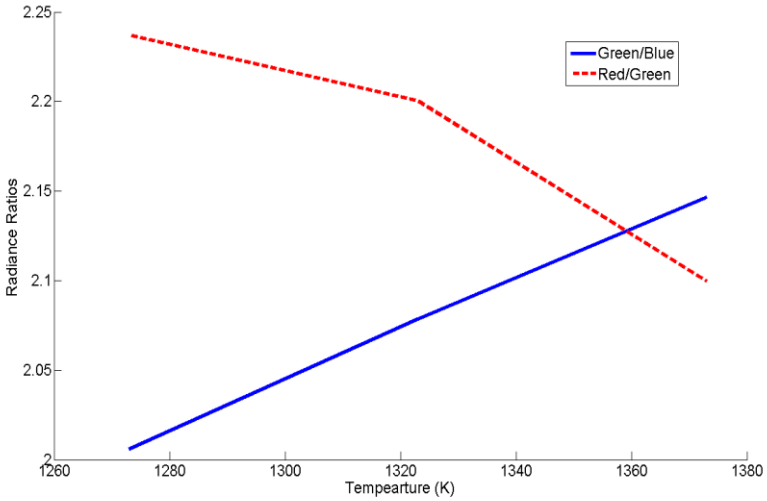

Figure 2.3 Spectral response ratios calculated at various blackbody temperatures

Analysis of the calculated correction coefficients shows that the Red/Green slope is exceptionally large and has the opposite sign predicted by the multi-color model. The Red/Green ratio's insensitivity to temperature shows that there are problems when implementing the two color pyrometry method with broadband filters. In contrast to the Red/Green ratio, the Green/Blue ratio trends with temperature, however, the trend is also much steeper that the curve predicted in **Figure 2.1**. To understand why there is a discrepancy between the laboratory data and the predictive model, an experiment was devised to characterize the spectral response of the FPA. By multiplying the spectral response of the FPA with the blackbody's spectral emission and then integrating over the curve, it is possible to simulate the counts reported by each color channel. A software model was then created to simulate the FPA's spectral response. As such, it is possible to predict the output values of the sensor at various blackbody temperatures. A detailed

description of the proposed experiment as well as the experimental results will be presented in the next two chapters. However, for the purposes of continuity, a brief description of the experimental results will be described here.

The result of this experiment shows that at the described temperatures, there is an increase in the blackbody spectral radiance emission as a function of temperature. However, there is not a significant shift in the distribution of the spectral radiance for either the green or red spectral regions. This effect reveals why the red/green ratio (illustrated in **Figure 2.3**) was insensitive to temperature. Furthermore, the integrated radiance in the blue channel is significantly lower than that measured by the green channel which causes the steep slope of the trend line at theses temperature ranges.

CHAPTER 3

MEASUREMENT OF THE SENSOR'S SPECTRAL RESPONSE

3.1. Design of Experiment

In order to determine the cause of the effects described in the previous chapter, the combined spectral response of the silicon CMOS array and color filters were measured. This was achieved manually using a halogen lamp and a monochromator to measure the sensor response which has proven to be an effective technique [**42**,**43**]. The monochromator has a ticker reading that reports the transmission wavelength. Over time, error builds up in the indicator reading and the system needs to be recalibrated. The monochromator was calibrated using a Helium Neon (HeNe) laser and an Optical Power Meter. The monochromator is run through several wavelengths near the operating wavelength of the HeNe laser (632.8 nm). The setup of this experiment is shown below in **Figure 3.1**.

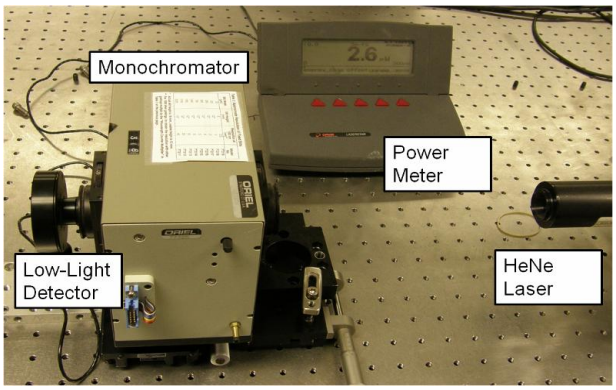

Figure 3.1 Monochromator calibration

Any error in the monochromator's wavelength indicator can be seen by plotting the reported wavelength versus the measured power. Though not shown, all data was collected under darkroom conditions with overhead lights turned off and a felt curtain surrounding the setup. The data that was produced by this experiment is presented below in **Table 3.1**. The experiment shows that there is approximately a 1.5 to 2 nm error in the monochromator's wavelength indicator. This error must be accounted for when measuring the sensor's spectral response.

Table 3.1 Optical power measurements of HeNe laser for monochromator calibration.

Wavelength Reported by Monochromator (nm)	**Power Meter Readout (μW)**
633.2	9.3500E-05
633.6	1.4880E-04
634	1.7750E-04
634.4	1.3010E-04
634.8	8.4300E-05
635.2	3.3800E-05
635.6	7.0000E-06

After calibration, the monochromator is integrated into a breadboard setup so that the combined spectral response can be measured. At this point, an objective lens was incorporated onto the camera, and thus some sort of intermediate image plane was necessary to carry out the measurements. This was further complicated by the fact that in order to achieve the most accurate spectral resolution, the input and output slit-widths of the monochromator were both set to 0.6 mm.

To solve this problem a 1^{o} Gaussian profile diffuser was placed directly after the monochromator's order sorting filter in front the output slit. The diffusers were used to broaden the monochromator's output beam so that the counts from several of the

camera's pixels could be averaged together at each wavelength. A second 5^{o} Gaussian profile diffuser was placed a few inches down the optical axis to serve as an object plane for the sensor.

An aluminum fold mirror was mounted inside of a flip mount and placed along the optical axis after the diffuser. Using the flip mirror, both the CMOS camera and a reference power meter can sequentially sample the beam at each wavelength. The manufacturer of the flip mount advertises a repeatability of better than 200 μrad. To characterize the mirror, two calibrated optical power meters were integrated into the setup after the flip mirror. One power meter was placed on the transmission leg of the setup. A second power meter was placed on the reflection leg. Measurements were taken by both power meters from 400 nm to 700 nm at regular intervals through the spectrum. The data collected from this experiment is shown below in **Table 3.2**. This data shows that the mirror's spectral reflectance is approximately uniform over the spectral range.

Table 3.2 Spectral reflectance measurements of metal mirror.

Wavelength (nm)	Reflection Measurement (Watts)	Transmission Measurement (Watts)
400	4.343E-08	5.249E-08
420	8.925E-08	7.330E-08
440	1.767E-07	1.136E-07
480	4.424E-07	2.242E-07
520	9.550E-07	4.202E-07
540	1.129E-06	5.119E-07
560	1.376E-06	6.167E-07
580	1.648E-06	7.348E-07
600	1.895E-06	8.102E-07
620	2.016E-06	8.627E-07
640	2.096E-06	9.297E-07
660	2.248E-06	9.620E-07
680	2.344E-06	1.002E-06
700	2.385E-06	1.055E-06

The power meter in the transmission leg was then replaced with the CMOS camera. With this setup, it was possible to step through the visible spectrum at regular intervals and measure the counts reported by each of the three color channels. The power meter in the reflection leg served as a reference detector to relate the counts reported by the camera to the actual power exiting the monochromator. This was necessary because the halogen source, though white in appearance, did not have a spectrally flat emission profile.

Note that since the multi-color method (described in the previous chapter) uses a ratio-based approach, only the relative spectral response of the sensor is needed. Therefore, no effort was made to characterize the spectral transmission profile of either diffuser as they are common to both the transmission and reflection legs. The spectral response of the CMOS sensor was then measured using the calibrated monochromator. The setup for this experiment is shown below in **Figure 3.2**.

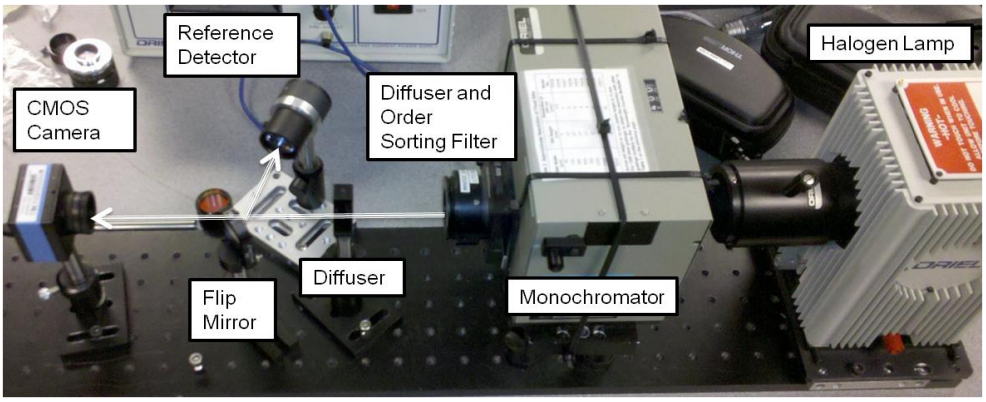

Figure 3.2 Spectral response measurement setup.

Monochromator measurements were taken from 400 nm to 700 nm at 10 nm intervals. The spectral output power of the halogen lamp was monitored with a calibrated Newport power meter on the reflection leg. Because two diffusers were

included in the experiment's optics train, an F# 1 singlet objective lens was mounted on the detector to ensure that the focused spot always under-filled the active area of the power meter over the entire waveband.

3.2. Spectral Response Measurements

From this experimental setup, it was possible to measure the normalized spectral responsivity curves of the camera's three color channels. Data was collected between 400 nm to 700 nm at 10 nm increments. This data collected from the setup is presented below in **Figure 3.3**.

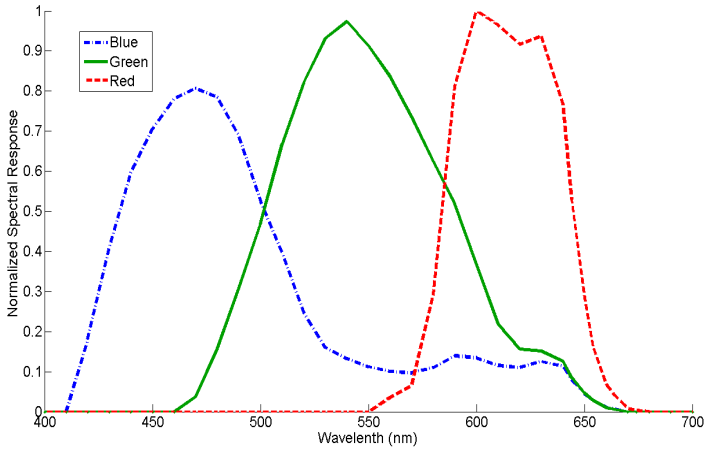

Figure 3.3 Measured spectral response of CMOS array.

Now that the measurement of the CMOS sensor's spectral response has been measured, it is now possible to model the sensor's performance for a variety of blackbody temperatures. Specifically, this model will allow for the investigation of the sensor's dynamic range to ensure it is sufficient for a wide range of blackbody temperatures. This evaluation is explained in greater detail in the following chapter.

To serve as a validation of the spectral response model, the imaging pyrometer will measure laboratory blackbody sources at incremental temperatures ranging from 1100 K to 2600 K. The spectral response model will be used to calculate the expected ratios between the three color channels and then comparing them to the actual ratios from the measured blackbody sources. Validation of the sensor's spectral response model will be achieved by showing an agreement between the measured color ratios and the theoretically predicted ratios. Once validated, the spectral response model can be used to determine why the measured color ratios were insensitive to changes in temperature (see **Figure 2.3**).

CHAPTER 4

MODELING THE SENSOR'S PERFORMANCE

4.1. Incorporating Planck's Blackbody Equation into the Sensor Model

Using the spectral response curves measured in the previous chapter, it is possible to simulate the spectral response of the camera multiplying these response curves with theoretical blackbody curves at various temperatures. This multiplication will reveal the spectral radiance distribution across each Bayer filter. The spectral response simulation reveals that at the lower temperature range, the increase in blackbody temperature does not cause a significant change in the shape of the spectral curves. However, an increase in temperature does cause an increase in the overall radiance emitted by the source. Thus, an increase in temperature will cause a shift in the location of the peak optical power in both the red and green filters, while virtually no shift occurs in the blue. This effect is due to the fact that the total optical power in the blue portion of the blackbody spectrum is roughly one and two orders of magnitude lower than the total optical power in the green and red spectral regions, respectively.

Planck's Blackbody Law predicts that the change in blackbody temperature will significantly increases the total flux emitted by the radiator as its temperature increases form 1273 K to 1373 K. However in this temperature range, the change in the blackbody curve is most significant near the red end of the spectrum as the peak of the curve shifts towards the blue when the temperature increases.

The measured spectral response for each of the three Bayer filters, shown above in **Figure 3.3**, was applied to Matlab's cubic spline interpolation function do generate a dense responsivity curves. The resulting interpolated data was then multiplying with theoretical blackbody curves at 1273 K and 1373 K in order to determine how the overall spectral radiance distribution shifts with temperature. Therefore, it is possible to simulate the normalized spectral radiance that is incident on the CMOS array for various blackbody temperatures. The temperatures of 1273 K and 1373 K were chosen because they are representative of the temperatures measured in **Section 2.2**.

Figure 4.1, shown below, is a plot of the measured spectral response curves of the CMOS array multiplied with the theoretical output of the Planck Blackbody Curve for a source at 1273 K and at 1373 K. Because there is such a large dynamic range along the blackbody spectrum at these temperatures, each of the three response curves has been normalized for comparison purposes.

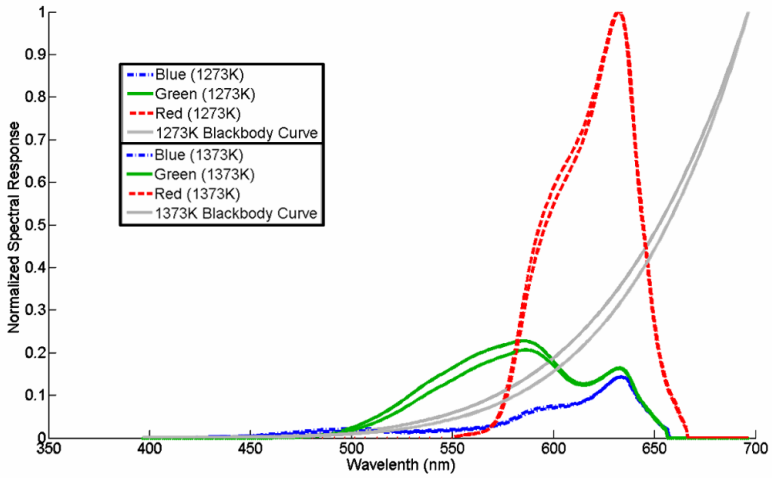

Figure 4.1 Multiplication of blackbody curve with spectral response of CMOS color filters.

This data shows that at these temperature ranges, there is not a significant shift in the distribution of the spectral radiance for the either the green or red color channels. This effect reveals why the red/green ratio (illustrated in **Figure 2.3**) was insensitive to temperature. Furthermore, the integrated radiance in the blue channel is significantly lower than that measured by the green channel which causes the steep slope of the trend line at theses temperature ranges. The pixel values reported by the camera are proportional to the integral of the curves shown in **Figure 4.1**. The functional form of this relationship is given below in **Equation 4.1**, where L_λ is the spectral radiance of the source, and $R(\lambda)$ is the responsivity of the detector at a given wavelength, $d\Omega$ is the instantaneous solid angle of each pixel, and dt is the incremental integration time of the sensor [**44**]. Strictly speaking, these integrals are indefinite, but for the purposes of this discussion the integral for each color channel will be bounded the limits of its associated Bayer filter.

$$
\begin{aligned}
Counts_{blue} &= \iiint \left[\int_{410nm}^{660nm} L_\lambda \cdot R(\lambda) \cdot d_\lambda \right] \cdot d\Omega \cdot dA \cdot dt \\
Counts_{green} &= \iiint \left[\int_{460nm}^{660nm} L_\lambda \cdot R(\lambda) \cdot d_\lambda \right] \cdot d\Omega \cdot dA \cdot dt \\
Counts_{red} &= \iiint \left[\int_{550nm}^{660nm} L_\lambda \cdot R(\lambda) \cdot d_\lambda \right] \cdot d\Omega \cdot dA \cdot dt
\end{aligned}
\qquad \textbf{(4.1)}
$$

It must be noted that no effort was taken to characterize the area or instantaneous solid if each individual pixel. This is because the multi-color method (presented in **Chapter 2**) deals strictly with ratios. Therefore, when calculating the ratios between any two color channels, these values are factored out; resulting in **Equation 4.2**, given below.

$$\frac{Counts_{red}}{Counts_{green}} = \frac{\int_{550nm}^{660nm} L_\lambda \cdot R(\lambda) \cdot d_\lambda}{\int_{460nm}^{660nm} L_\lambda \cdot R(\lambda) \cdot d_\lambda}, \qquad \frac{Counts_{green}}{Counts_{blue}} = \frac{\int_{460nm}^{660nm} L_\lambda \cdot R(\lambda) \cdot d_\lambda}{\int_{410nm}^{660nm} L_\lambda \cdot R(\lambda) \cdot d_\lambda} \tag{4.2}$$

4.2. Analysis of the Sensor's Dynamic Range

By using this computer model of the sensor's spectral response, effort was made to characterize the sensor's dynamic range. This analysis is to assess how the sensor is expected to perform against various blackbody curves in order to define a high and low temperature range in which the sensor can operate. Hydrocarbon flame temperatures can be expected to occupy a region from 1600 K to just under 3000 K [**45**].

Characterization of the sensor's dynamic range can be achieved by extending the concept of the multi-color method to the ratio between the red and blue color channels, as shown in **Equation 4.3**. This ratio represents the highest and lowest count, as determined in the analysis shown in the previous section. Therefore, to evaluate the sensor's Signal to Noise Ratio (SNR) at various temperatures, the spectral response model is used calculate the ratio between these two color channels using the right hand side of **Equation 4.3**.

$$\frac{Counts_{red}}{Counts_{blue}} = \frac{\int_{550nm}^{660nm} L_\lambda \cdot R(\lambda) \cdot d_\lambda}{\int_{4100nm}^{660nm} L_\lambda \cdot R(\lambda) \cdot d_\lambda} \tag{4.3}$$

At approximately 2600 K, the spectral response model predicts a ratio of the red to blue channel is 2.2544. If the red channel count value is just under saturation at a pixel

value of 250 counts, then this red/blue ratio predicts a blue channel value of (250/2.2544)=110.8934 counts. This calculation indicates that for blackbody temperatures at the higher end of the region, the sensor will have sufficient SNR.

However, what is of most concern is the sensor's response to flame radiation at lower end temperatures. When the blackbody temperature in the sensor model is lowered to 1400 K, and the red channel is assumed to have a value of 250 counts, then the blue channel value is predicted to report approximately 50 counts. It must also be considered that the blue channel has an average constant background value of 10.0436 counts. This background value has been shown to be constant regardless of the cameras exposure time when there is zero electronic gain applied to the FPA. Through this analysis, it is predicted that the blue channel will be only 30 counts above the noise floor at 1400 K (assuming that a minimum SNR of 2 is required). An illustration of this simulated analysis is provided in **Figure 4.2**.

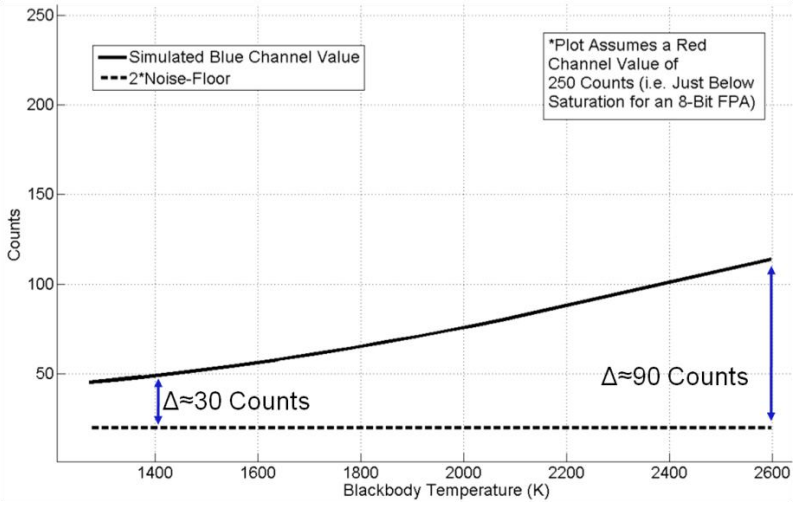

Figure 4.2 Simulated SNR of the CMOS sensor.

Outside this 30-count window, either the blue channel will be in the noise, or the red channel will be saturated. If either event occurs, the sensor will no longer be able to

report meaningful data about the portion(s) of the flame outside these accepted count values. Given the inherently variability of free burning flames, the SNR of the CMOS camera is considered to be insufficient at the lower temperatures. To fully investigate lower temperature blackbodies, a solution is needed to account for the disparity in power distributions between the blue and red channels.

4.3. Overcoming the Sensor's Dynamic Range

In order to improve the sensor's dynamic range, it is first necessary to investigate the spectral radiance distribution of the blackbody curve at these lower temperatures. From **Equation 2.1**, at 1273 K, the radiance emitted by a theoretical blackbody radiator at 620 nm is calculated to be 50.7473 times the radiance emitted at 480 nm. By comparison, at 2700 K, the spectral radiance emitted by a theoretical blackbody radiator at 620 nm is calculated to be 3.4122 times the radiance emitted at 480 nm. **Figure 4.3** to help illustrate how significantly the blackbody curve changes with respect to temperature.

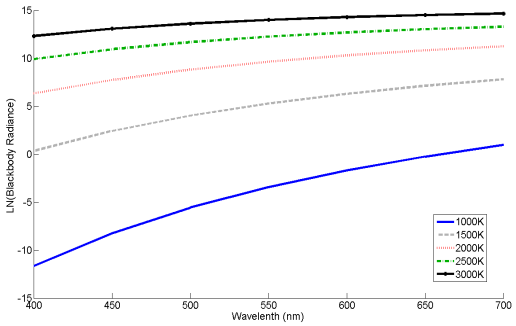

Figure 4.3 Radiance emission vs. wavelength

From this analysis, it can be seen that there is a significant change in spectral radiance distribution over the temperature range, and a method is needed to allow the CMOS camera to accommodate this effect.

To overcome this, an IR cut-filter (also referred to as a low pass filter) was included in the camera's optics train. An IR cut-filter is an ideal solution to the dynamic range problem presented by the CMOS sensor because it will allow the total integrated radiance incident on the red channel to be significantly reduced. The inclusion of an IR cut-filter is a proven solution and many scientific camera manufacturers integrate these filters into the camera's hardware. Typically, these filters have a cut-off wavelength between 650 nm and 700 nm in order to improve the performance of the FPA's Bayer filters [**46**]. It has also been shown that sensor's performance can be improved by extending the cut-off wavelength into the visible spectrum [**47**,**48**,**49**]. The alternative solution to using a cut-filter would be to electronically gain-up the blue channel. However, with the channel having a large background value of approximately 10 counts, this solution will also raise the sensor's noise floor. Given these two options, the cut-filter approach was selected to improve the sensor's dynamic range.

The optimal cut-off wavelength was chosen by first researching commercially available filters. This industry survey was designed to maintain the low cost goal set forth in the original sensor description. Several candidate cut-off wavelengths were identified and the transmission profile of each filter was approximated in Matlab based on information published on the manufacturers' websites. The transmission profiles of each candidate filter were integrated into the software model of the camera's spectral response. **Equation 4.4**, shown below, is an expansion of **Equation 4.1** to include the spectral transmission profile (T_λ) of the cut-off filter being simulated. Though this

applies to all three color channels, the cut-off filter will have the greatest effect on the red channel.

$$Counts_{red} = \iiint \left[\int_{550nm}^{\lambda-Cut-Off} L_\lambda \cdot R(\lambda) \cdot T(\lambda) \cdot d_\lambda \right] \cdot d\Omega \cdot dA \cdot dt \qquad \textbf{(4.4)}$$

After testing several candidate cut-off filters, 600 nm was selected as optimal cut-off wavelength. Incorporating such a filter into the camera's optics train effectively reduces the total integrated power on the red channel by approximately 75%. After selecting the cut-off wavelength, a sample filter was obtained and its spectral transmission profile was measured using the Ocean Optics HR2000+ fiber-optic spectrometer. The setup for this measurement is shown below in **Figure 4.4.**

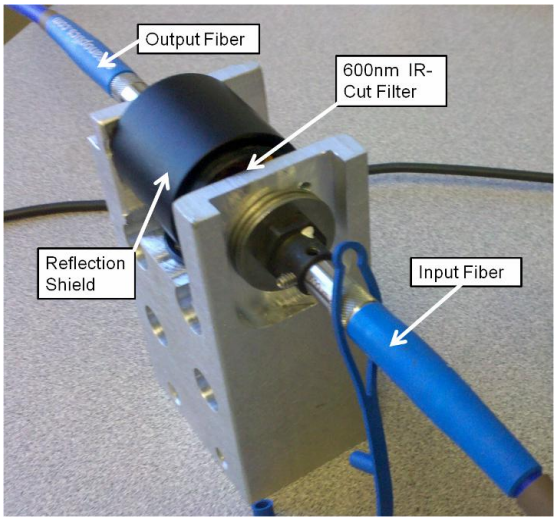

Figure 4.4 Measurement of the IR cut-filter's spectral transmission profile

The filter was placed inside a lens tube to block out ambient light and to ensure that the optical axis of the measurement fibers was normal to front surface of the filter.

The measured transmission profile of the cut-off filter is shown below in **Figure 4.5**. Once the filter's exact spectral transmission profile was measured, this data was integrated into the camera's spectral response model using **Equation 4.4**.

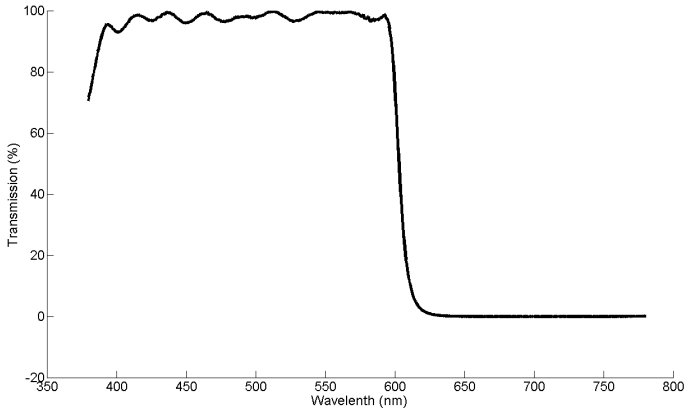

Figure 4.5. IR cut-filter's spectral transmission profile

A layout of the sensor's optics train is provided below in **Figure 4.6**. Note that the filter was placed in front of the objective lens for convenience.

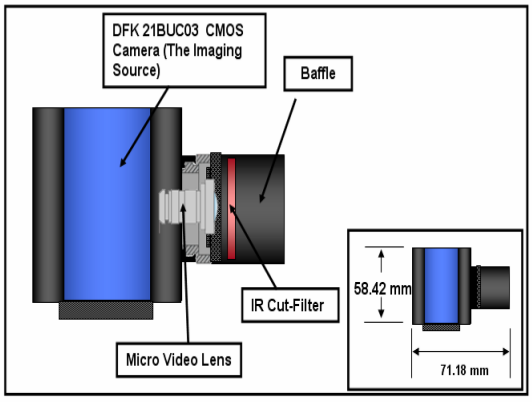

Figure 4.6 Imaging pyrometer with integrated IR cut-filter.

Future research will consider a method to directly integrate the filter into the optics train. This will allow the next generation sensor to accommodate large objective

lenses with variable focus and zoom capabilities. **Figure 4.7** shows the measured spectral response of the CMOS sensor multiplied by the IR cut filter's transmission profile. Note how these curves compare to those shown in **Figure 3.3**.

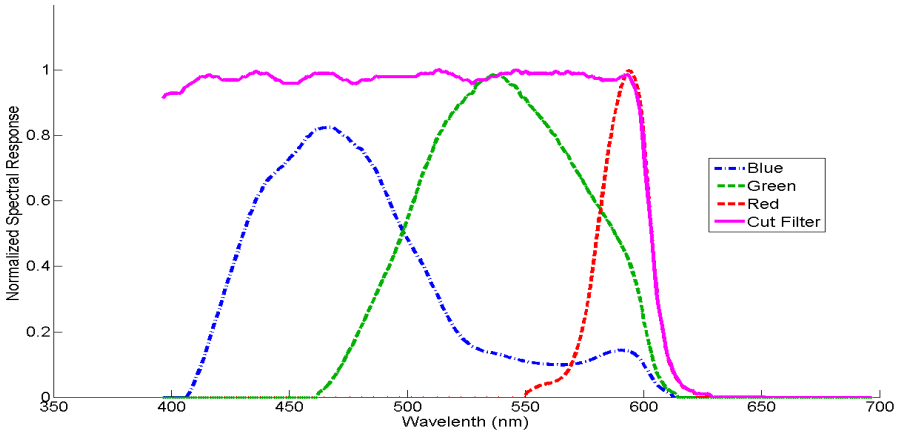

Figure 4.7 CMOS spectral response overlaid with IR cut-filter.

The inclusion of the of the IR cut filter, the experiment performed in **Section 2.3** must be repeated. At 1273 K, the responsivity model for the CMOS camera now predicts the red over blue ratio to be 3.2742. If again, it is assumed that the red channel is just under saturation at a value of 250 counts, then this ratio corresponds to a blue channel value of 76.3551. Because the IR cut-filter effectively decreases the total power detected by the red channel by 75%, it is now possible to significantly increase the camera's exposure time. This increase in exposure time allows to blue channel to dwell on the source longer and report a higher pixel count. Increasing the sensor's exposure time serves to further improve the overall SNR, however, there is also the increased risk of motion blur.

Due to the transient nature of free burning flames, there is a risk of introducing motion blur into the flame data when the exposure time is increased. This effect will naturally be most pronounced at the edges of the fire where the brighter flame will blur with darker background imagery. Techniques exist for removing motion blur and have proven effective for many applications [**50**]. While the implementation of these image processing techniques may prove necessary for certain burn conditions, they will not be employed within this scope of work presented here. As an alternative, this paper will present a calibration algorithm that seeks to mitigate the influence of the background imagery on the flame measurements. A detailed description of this approach will be presented as a method for identifying and evaluating translucent potions of the flame.

To further show the effects of the IR cut-filter, the experiment was repeated at 2600 K. At this blackbody temperature, the red over blue ratio is predicted to be 0.9786, indicating that at the upper end of the anticipated flame temperatures, the pixel counts reported by the blue channel will actually exceed those reported by the red channel. This ensures that the by including the IR cut-filter in the camera's optics train, the CMOS sensor will now have sufficient dynamic range to cover any flame temperature between 1600 K and 3000 K.

Figure 4.8, shown below, is a plot of the effective spectral response curves of the CMOS array combined with the IR cut-filter and multiplied with the theoretical output of the Planck Blackbody Curve for a source at 1273 K and at 1373 K. Because there is such a large dynamic range along the blackbody spectrum at these temperatures, each of the three response curves have been normalized for comparison purposes.

Analyzing the simulation, it can be seen that the power distribution profile is greatly improved by the IR cut filter for the lower blackbody temperatures. Additionally,

the simulation also shows that there is a noticeable shift in the green channel, and only a slight shift in the red channel. Therefore, in addition to improving the dynamic range of the sensor, the IR cut filter allows a slight shift in the green channel's power distribution to be significant enough to change the green-over-red color ratio. Thus, with the inclusion of the IR cut-filter, the red/green color ratio is now sensitive to changes in temperature. Furthermore, with the filter in place, all three color channels are significantly above the noise floor regardless of the temperature. Therefore, it is now possible to develop a calibration algorithm that utilizes all three color channels over the full temperature range. A calibration method that incorporates all three color channels will be described in next chapter.

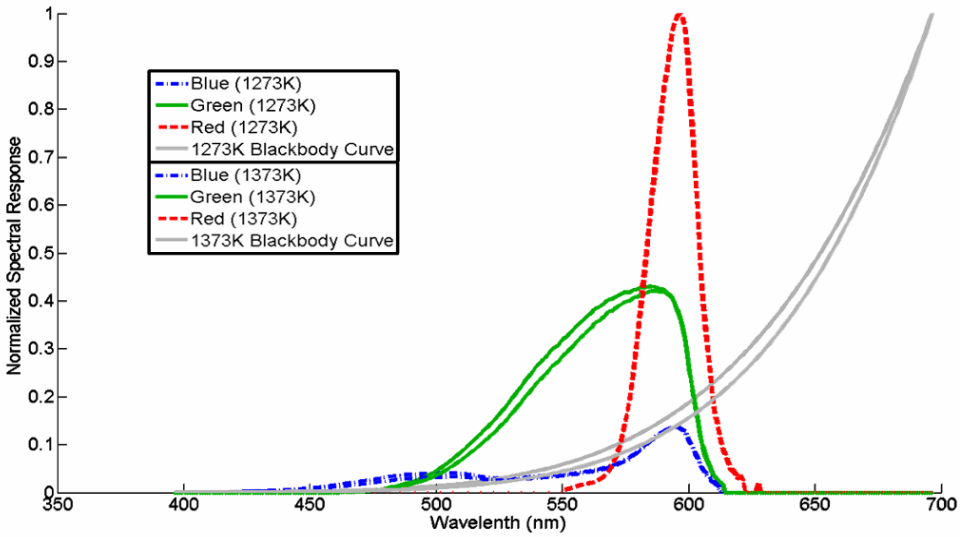

Figure 4.8 Multiplication of blackbody curve with spectral response of CMOS color filters with integrated IR cut filter.

CHAPTER 5

CALIBRATION OF THE SENSOR

5.1. Calibration Setup

Before calibrating the pyrometer, a series of laboratory blackbody measurements was taken in order to fully validate the spectral response model of the CMOS sensor. These blackbody measurements were designed to cover the full range of temperatures that are expected for hydrocarbon flames. As previously mentioned, the spectral response measurements of the sensor were only concerned with relative response of the three color channels. Therefore, any validation of the spectral response model must be based on evaluating the ratios between the color channels.

At each source temperature, multiple pixels from each of the three color channels were recorded and used to generate a trend line for both the red-over-green and the green-over-blue ratios. These same blackbody temperatures are repeated using the camera's spectral response model for comparison purposes. The full ranges of blackbody measurements were taken using two separate sources.

The first source was a Mikron M360 laboratory blackbody source to cover the lower end of the temperature range. This produced a uniform blackbody temperature profile between 1173 K and 1373 K. The source reported its temperature via a calibrated thermocouple which was pre-installed by the manufacturer. However, to obtain blackbody measurements for the higher end of the spectrum, a different method was required. No available blackbody source with an integrated thermocouple was available

to collect blackbody measurements. To overcome this problem, research was done to find simple blackbody radiators with as uniform an emissivity as possible.

Ultimately, a 60 W incandescent bulb with a frosted spherical glass dome was selected as the high temperature calibration source. The wider cross-section allows a large number of pixels from all three color channels to be averaged for the calibration measurement thus reducing the overall noise in the measurement.

The emissivity of the bulb was found to be uniform over the visible waveband and the spectral emission could be modeled as a greybody. Whether or not the emissivity of the bulb had a value equal to 1 was irrelevant. The only point of concern was that the emissivity was uniform across the visible waveband. This approach meant that the bulb's color temperature, rather than the actual temperature of its filament could be used to calibrate the pyrometer at the higher temperatures. Because the bulb's emissivity was uniform, the color channel ratio approach would make the source appear to the sensor as if it were a true blackbody radiator.

The incandescent bulb was powered by a bench top power supply with a variable voltage capability. By raising the voltage level of the power supply, the bulb's current draw was increased which effectively raised the color temperature of the filament. At each voltage setting, the bulb was measured simultaneously using the SP-100 spectroradiometer and the imaging pyrometer. The SP-100 was mounted on a breadboard setup approximately three feet from the bulb. The SP-100 features a circular laser marker that designates what portion of the scene is viewed by the sensor. The laser designator was activated and aligned with the center of the incandescent bulb. Once aligned, the imaging pyrometer was mounted next to the spectrometer and boresighted so that the laser designator was centered within the pyrometer's FOV in both dimensions.

This centering of the FOV was done in order to avoid any potential off-axis effects with the IR cut-filter. The camera has a region of interest (ROI) functionality that allows only a specified portion of the scene to be saved to file. The ROI was selected so that only the portion of the bulb designated by the SP-100 was recorded for each calibration measurement. A screen capture of the scene as viewed by the pyrometer is shown below in **Figure 5.1**. Because the SP-100 uses a HeNe laser for the designator spot, the alignment was performed before the IR cut filter was integrated into the camera.

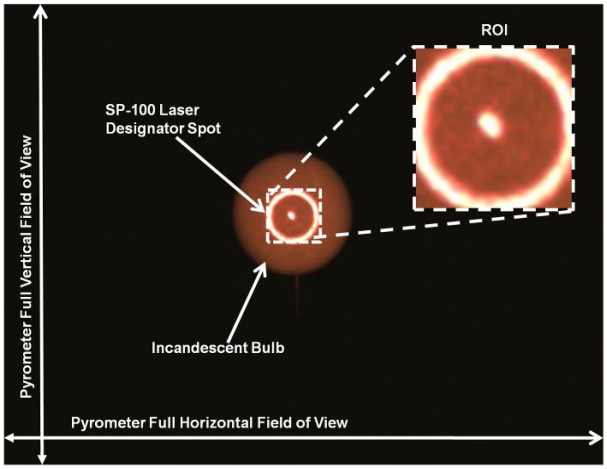

Figure 5.1 Darkroom measurement of incandescent bulb as seen by the pyrometer.

After the two sensors were aligned, the IR cut filter was then mounted inside a threaded lens tub and attached to the pyrometer. In addition to housing the filter, the lens tub was also designed to be long enough to act as an effective sun shield but short enough to not obstruct the FOV in either dimension. The sun shield will prove useful during the sensor's field test measurements, described in the next chapter**.** The measurement setup for collecting the spectral emission profile of the 100 Watt bulb is shown below in **Figure 5.2**.

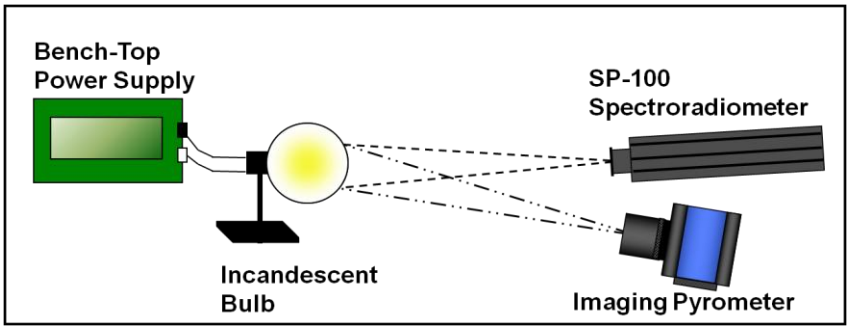

Figure 5.2 Measurement of incandescent bulb emission spectrum

5.2. Calculating the Temperature of the Measured Curve

The SP-100 and the imaging pyrometer measure the bulb simultaneously, taking a series measurements over a period of approximately 1 to 10 minutes. Lower voltage settings for the glass bulb required long exposure times, while higher voltages required shorter exposure settings. The SP-100 used an internal auto-exposure algorithm and reported absolute radiance measurements. By contrast, the exposure time of the imaging pyrometer was manually adjusted for each voltage level such that the maximum pixel count was just under saturation. At each voltage level, the pyrometer collected a movie of 100 frames and the SP-100 collected 30 measurements. Measurements were saved to file using the acquisition software that was included with each sensor. The series of measurements taken at each voltage level were averaged together to lower the noise floor.

Figure 5.3 shows an example average of 30 measurements of the spectral output of a 60 watt bulb collected with the SP-100. The data shows that the source's spectral emission profile behave like a blackbody within the waveband of interest. Furthermore, the standard deviation plot verifies that source is stable over the measurement interval. The fit error between 400 nm and 780 nm is 2.24%.

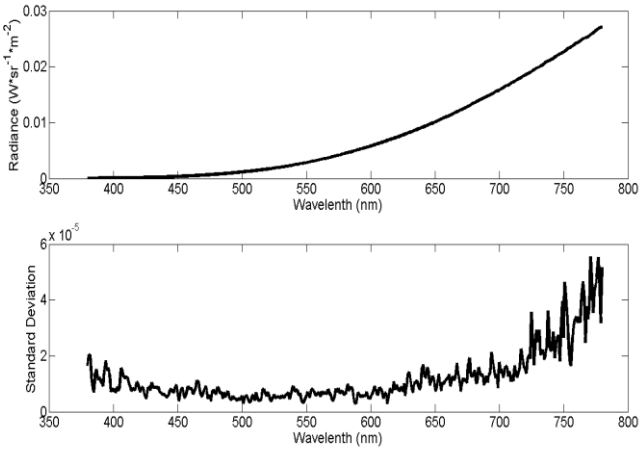

Figure 5.3 Example measurement of a 60 Watt Incandescent Bulb

An explanation will now be given for how these measured spectral radiance curves to calculate the temperature of the apparent temperature of the source. To accomplish this, an algorithm was developed to determine the corresponding temperature necessary to generate the blackbody curve. This is done by sequentially calculating every theoretical blackbody curve generated by temperatures from 700 K to 6000 K. For each temperature, the natural log of the measured integrated radiance (L) versus the natural log of the theoretical radiance was fit to a linear equation, as shown below in **Equation 5.1** over the visible waveband.

$$LN(L-Theoretical) = M \cdot LN(L-Measured) + B \qquad \textbf{(5.1)}$$

Here, M is the slope and B is the D.C. offset. From M, a value M^* can be calculated where M^*=abs (1-M). Employing this algorithm, the temperature that produces the lowest value of M^* is necessarily the corresponding color temperature that

generated the measured spectral curve. Using the data presented in **Figure 5.3,** the resulting temperature versus M^* curve is shown below in **Figure 5.4**.

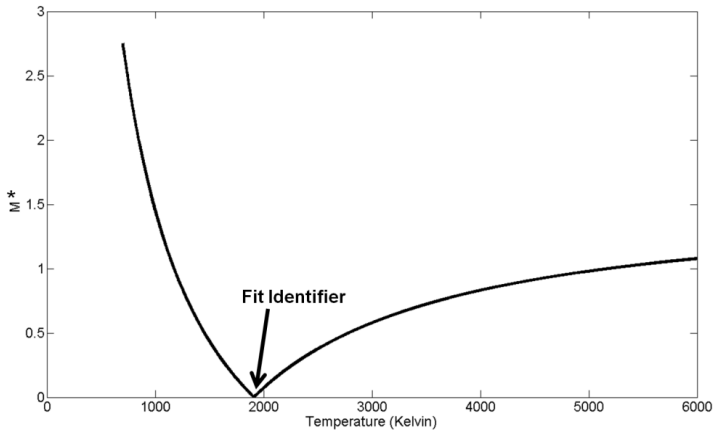

Figure 5.4 Temperature vs. M^*

A plot of the measured curve compared to the theoretical curve predicted by the temperature calculation algorithm is presented in **Figure 5.5.** The percent fit error is also presented in the figure. Note that there is a significant percent error in the curve fit below 400 nm. The cause of this fit error stems from the fact that the spectral emittance in this region is approaching the noise floor of the sensor. Additionally, there is a noticeable deviation between the measured and theoretical blackbody curves for the spectral range above 700 nm. This deviation is considered acceptable as it is outside the waveband of interest. What this experiment shows is that the apparent source temperature predicted by the curve fit algorithm produces a theoretical blackbody curve that closely matches the measured curve. Therefore, this method for determining the apparent temperature of the source has been verified.

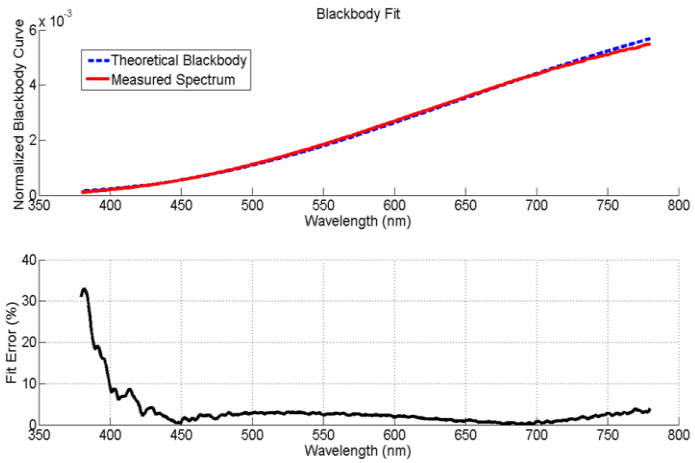

Figure 5.5 Measured spectral emission of incandescent bulb vs. theoretical blackbody curve at the predicted temperature (top) and fit error between the two curves (bottom).

This blackbody fit algorithm was applied to all the incandescent bulb measurements to produce the data previously shown below **Table 5.1**, which outlines the relationship between apparent temperature of the source, and the supply voltage. The incandescent bulb measurements combined with the laboratory blackbody measurements are now a sufficient set of blackbody data to cover the expected range of flame temperatures. As a final test, the data from these blackbody measurements will be used to validate the spectral response model of the imaging pyrometer from 1273 K to 2634 K.

Table 5.1 Voltage versus apparent color temperature of bulb.

Power Supply Setting (Volts)	Temperature (K)
22	1464
28	1560
32	1638
36	1714
40	1786
44	1850
48	1910
52	1966
56	2020
60	2074
AC Outlet Used	2598

5.3. Validation of the Spectral Response Model

The blackbody data measured in the laboratory will serve to verify the spectral response model of the pyrometry sensor (discussed in the previous chapter). Using **Equation 4.2**, the ratio between the red and green cannels and the ratio between the green and blue channels will be predicted by the spectral response model. These ratios will then be compared to those measured by the pyrometer at the various blackbody temperatures. A reminder will be given that the software model employees a cubic spline interpolation followed by a trapezoidal numerical integration to approximate a true analytical integration.

Figure 5.6, shown below, plots the ratio measured by the sensor overlaid with the ratios predicted by the spectral response model. This data shows that the spectral response model closely matches the ratios measured by the pyrometer over the entire temperature range.

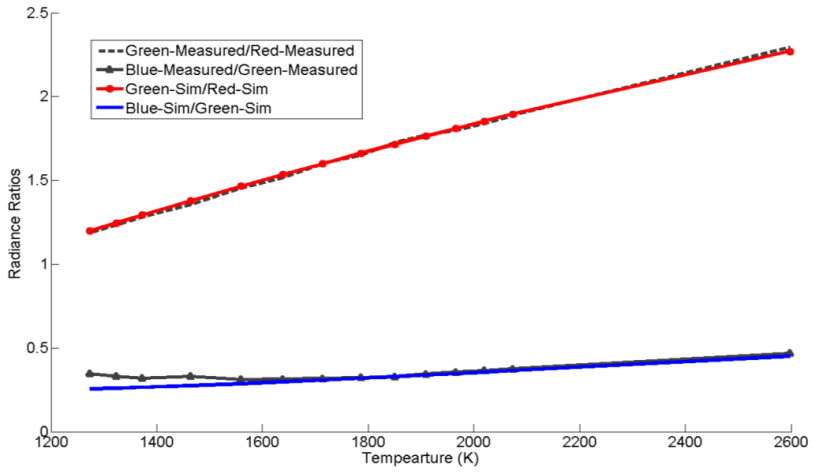

Figure 5.6 Measured versus predicted color channel ratios

The measured blue-over-green ratio slightly deviates from the predicted ratio for the lower range blackbody temperatures. The cause of this deviation is due to an over prediction by the model of the blue channel for these lower temperatures. This effect occurs in the lower temperature range because the emitted spectral flux at the lower end of the blue waveband is below the camera's minimum response value, resulting in a lower count value than that predicted by the model.

5.4. Calibration Algorithms

In the previous section, blackbody reference measurements were collected to verify the accuracy of the spectral response model. With the model now verified, it is possible to analyze the spectral power distribution incident on the FPA for the full range of temperature. This data will prove instrumental in developing a data reduction algorithm that utilizes all three color channels in order to calibrate the sensor. Additionally, once a calibration algorithm has been identified, the same blackbody reference measurements can be used to fully validate the accuracy of the calibration algorithm. **Figure 5.7**, shown below, plots the normalized power distributions of all three color channels as well as the associate blackbody curve profile for several flame temperatures within the range of interest.

This analysis shows that with the addition of the IR cut-filter, the green channel now contains the dominant integrated spectral radiance. Further analysis of the data also reveals that the green channel is more sensitive to temperature changes than the red channel. From this observation, it was concluded that these two factors should be utilized when developing a calibration data algorithm. A detailed description of two calibration algorithms developed by the author is presented in the next section.

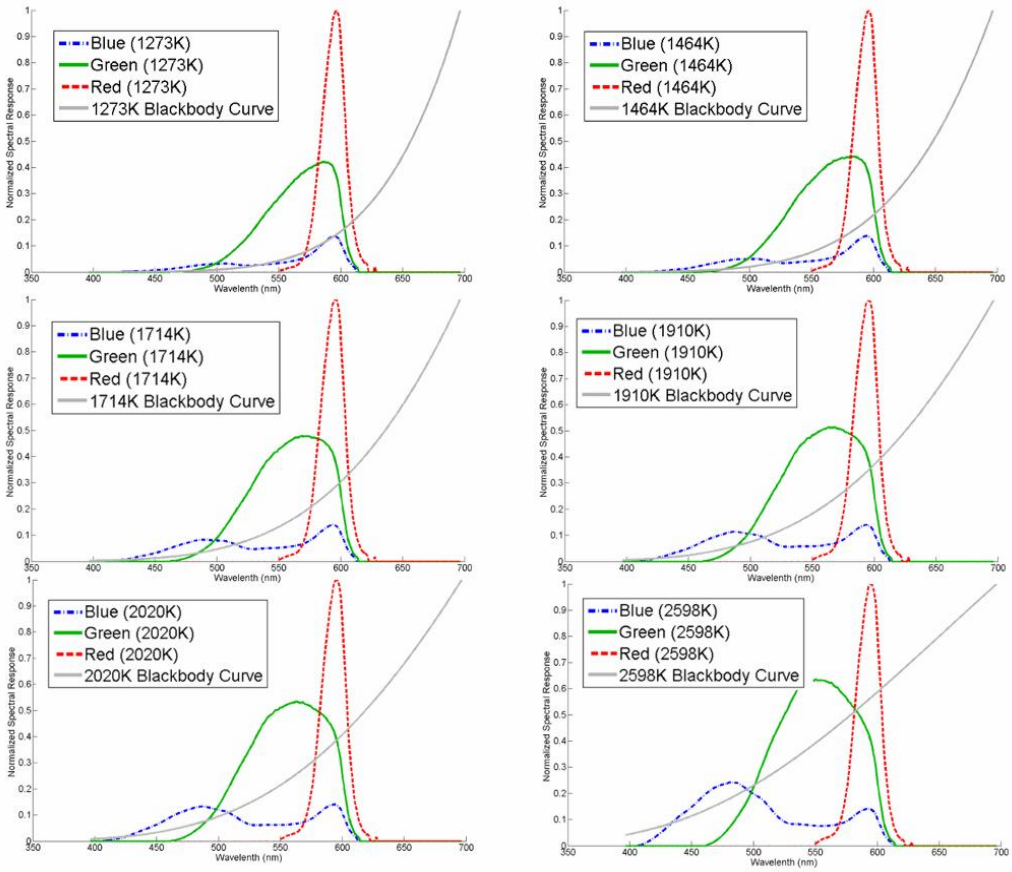

Figure 5.7 1273 K to 2598 K power distribution

5.4.1. Ratio Method

From this data, two observations where made which ultimately led to the development of a robust calibration algorithm. First, with the addition of the IR cut filter, any of the two color channel ratios are shown to be sensitive to changes in temperatures, as shown in **Figure 5.6.** Therefore, it can be concluded that an algorithm which incorporates all three color channels will also be sensitive to changes in temperature and should serve at the basis for any calibration algorithm. By iteratively testing representative flame data sets, two separate candidate algorithms were developed that utilize all three color channels. The first approach is a ratio based algorithm and is

described below in **Equation 5.2**. This algorithm was developed by the author and will be referred to as the ratio method.

$$Ratio = \frac{Blue + Green}{\mathrm{Re}\, d} \tag{5.2}$$

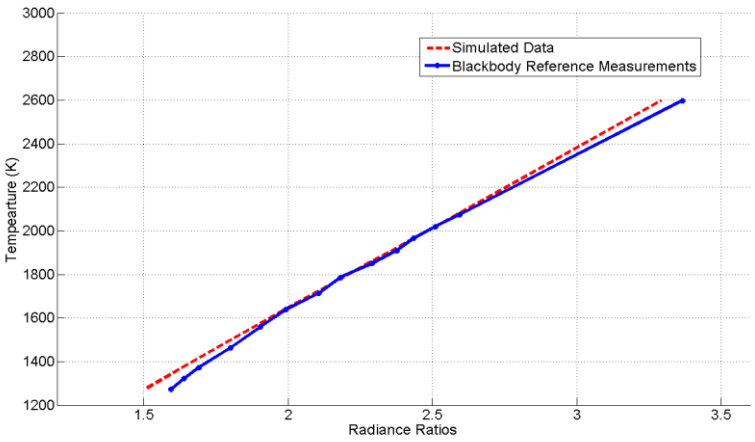

Figure 5.8 The color channel ratio method

5.4.2. Polynomial Derivative Method

This first algorithm is not considered to be novel as it is simply an extension of the multi-color method which has been employed for almost eighty years. However, the results of this algorithm are presented to serve as a performance baseline for comparative purposes. The remainder of this chapter will describe a calibration algorithm which is truly novel and will be shown to be more robust than a simple ratio-based multi-color method.

The second algorithm is based on the idea that the integrated flux measured by the green channel is always greater than the flux measured in either that of the blue or the red over the entire temperature range. In other words, the green channel will always report higher counts than the red or blue channels. This statement assumes the presence of the

previously discussed IR cut-filter. Model prediction was confirmed by the data shown in **Figure 5.9**.

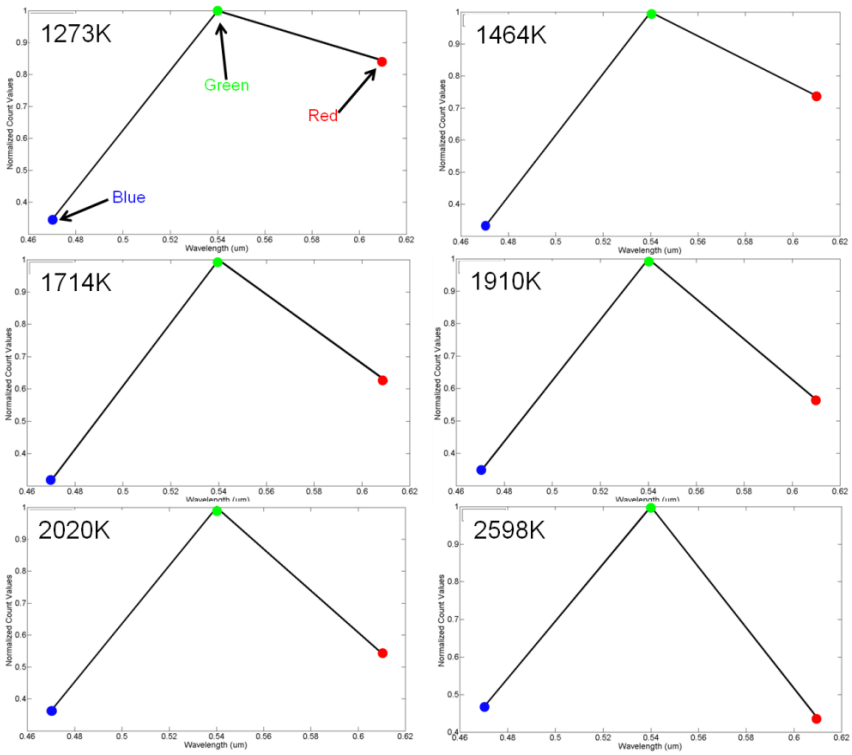

Figure 5.9 Normalized count values vs. bandpass filter center wavelength for several measured blackbody source temperatures.

The above figure plots the measured counts from all three color channels normalized by the green channel for several blackbody temperatures. The green channel is used to normalize the values because it has already been shown that this is always the channel highest reported counts. As shown in **Equation 4.1**, the pixel count reported by the camera is proportional to the integrated flux over the bandpass filter for each color channel. In effect, the data presented in **Figure 5.9** is equivalent to applying the method described in **Equation 4.1** to the spectral response curves presented in **Figure 5.7**. Thus, the counts reported by the three color channels report the total flux distribution emitted

by the source across the visible waveband. Furthermore, it is clear that this distribution changes as a function of temperature. Therefore, a calibration algorithm must be developed that can effectively monitor this distribution and relate it to the source temperature.

An argument can be made that the ratio method algorithm (presented earlier in this section) is an adequate technique for monitoring this distribution. For one, the ratio method does not account for the translucent regions of the flame. For areas with high translucence, the scene background bleeds through the flame and becomes visible. Pixels that subtend these portions of the image will report count values which are the summation of the flame emission and the background reflection. The functional form of this effect is shown in **Equation 5.3**. These background regions contribute to the pixels' count values; acting as a DC offset to the flame emission. For the ratio method, the introduction of these DC offsets will cause a skew in the temperature prediction.

$$Counts = \iiint \left[\int_{\lambda 1}^{\lambda 2} \left[L_\lambda + Background(\lambda) \right] \cdot R(\lambda) \cdot d_\lambda \right] \cdot d\Omega \cdot dA \cdot dt \qquad \textbf{(5.3)}$$

It is possible that these background values could be removed by subtracting a pre-flame background image. However, this approach is unappealing for three reasons. The first reason is that the sensor is assumed to be a fieldable instrument. A background removal approach would require the sensor to continually update the background image before the flame event to account for changes in lighting conditions. Second, such an approach cannot account for changes in lighting once the flame event has occurred. Third, and most significant, only those portions of the flame where the flame is

translucent require the background subtraction. For those portions of the flame where there is sufficient flame production, a background subtraction will apply an artificial DC offset to the image. Therefore, it must be concluded that the multi-color approach is not sufficient to accommodate flame translucent and an alternative algorithm is needed.

With this in mind, a unique calibration algorithm was developed to measure the flux distribution reported by the sensor. For this algorithm, the count values measured by the each color channel are referenced to the center wavelength of their respective Bayer filter. The data previously presented in **Figure 5.9** is an illustration of this approach.

These curves can be fitted to a second order polynomial because there are three color channels (i.e., three data points per pixel). Since the normalized red and blue channels change with respect to temperature, then the peak of the polynomial curve will also change with temperature. The core principle proposed by this algorithm is that the peak of the second-order polynomial curve will can be related to flame temperature.

The peak of the curve can be easily calculated by finding where the curve's first derivative is equal to zero. Each frame from the camera is effectively a MxNx3 matrix, where M and N are the number of row and columns in the image, respectively. To quickly calculate the curve peak for each pixel, the image is first turned into a 3x(M*N) matrix which is then multiplied by the inverse of the Vandermonde Matrix [**51**,**52**]. This approach calculates the polynomial coefficients for each pixel, as shown in **Equation 5.4** [**53**]. The Vandermonde Matrix is populated using the center wavelengths (μm) of the three Bayer filters.

Using the polynomial coefficients, the peak of the second-order curve can be easily calculated by finding where the curve's first derivative is equal to zero. The polynomial expression is shown in **Equation 5.5a**, and the method for calculating the

peak of the curve is given by **Equation 5.5b**. Since a red, green, and blue value is associated with each pixel, it is therefore possible to calculate temperature on a pixel-by-pixel basis. This algorithm is referred to as the derivative method and is presented as an advancement of the state of the art. This second method is applied to the blackbody reference measurements, and the resulting curve is shown below in **Figure 5.10**.

$$\begin{bmatrix} a_2 \\ a_1 \\ a_0 \end{bmatrix} = inv\left(\begin{bmatrix} .61^2 & .61^1 & .61^0 \\ .54^2 & .54^1 & .54^0 \\ .47^2 & .47^1 & .47^0 \end{bmatrix}\right) * \begin{bmatrix} \mathrm{Re}\,d-Counts_{1,1} & \mathrm{Re}\,d-Counts_{1,2} & \mathrm{Re}\,d-Counts_{m,n} \\ Green-Counts_{1,1} & Green-Counts_{1,2} & Green-Counts_{m,n} \\ Blue-Counts_{1,1} & Blue-Counts_{1,2} & Blue-Counts_{m,n} \end{bmatrix} \quad \textbf{(5.4)}$$

$$\text{a)} \quad counts = a_2 \cdot \lambda^2 + a_1 \cdot \lambda + a_0, \quad \text{b)} \ \lambda_{peak} = \frac{-a_1}{2 \cdot a_2} \quad \textbf{(5.5)}$$

As was previously discussed in this section, the first ratio-based algorithm was unable account for translucent regions of the flame. It was determined that the background values acted like DC components and skewed calculated ratios. This effect is especially significant for efficient burning fuels where there is low soot production. By comparison, when employing the polynomial derivative algorithm, the count values for the three color channels are fit to a second order polynomial and the peak of the polynomial is related to temperature. As shown in **Equation 5.5a,** this background DC component denoted as a_0. By taking the first derivative of the polynomial, as presented in **Equation 5.5b**, this DC component is zeroed out. This of course assumes that the variance in the background component across the three color channels is small compared to flame emission. Given that the strength of the carbon soot's absorptive constant is equal to its emissivity, it is a safe assumption that this will be the case.

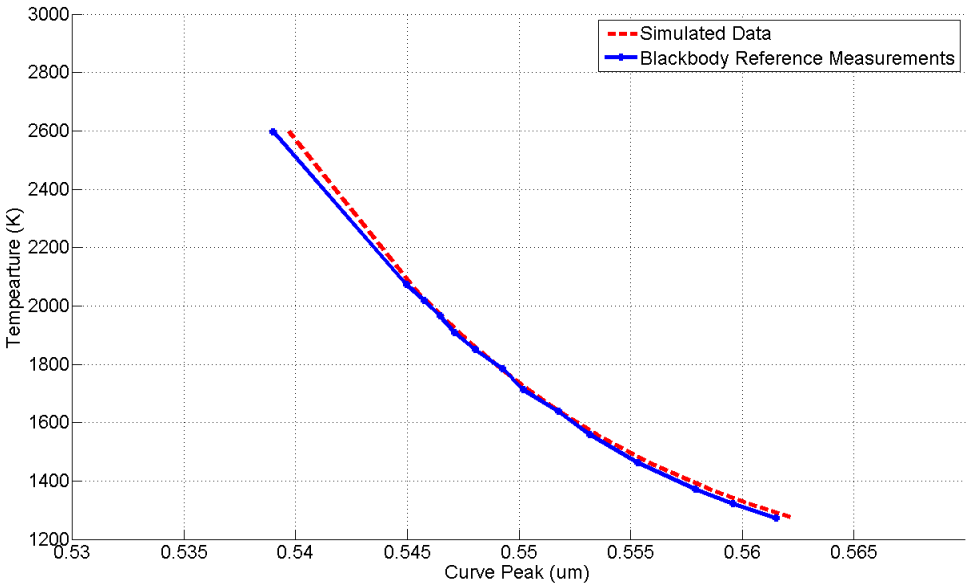

Figure 5.10 Curve peak versus temperature using the derivative method

In both calibration algorithms, it can be seen that there is a slight discrepancy between the blackbody reference measurement and the curves predicted by the spectral response simulation. This discrepancy can be explained by the compounded error of the monochromator, reference power meter, and the SP-100 spectroradiometer. This error has proven acceptable since the spectral response simulation was intended to understand the underlying performance of the camera in order to develop a calibration algorithm. Now that two potential calibration algorithms have been identified, the blackbody calibration measurements will be used to generate the calibration curve, rather than those curves generated by the spectral response model. For both algorithms, the blackbody reference measurements are fitted to a 6^{th} order polynomial curve in order to interpolate between the calibration measurements. This high order polynomial serves as the method for calculating temperature based on the trendline. In the following chapter, field test data will be collected and analyzed to test the accuracy of the two calibration methods.

Through an investigation of both presented algorithms, it can be seen that both methods are immune to flame emissivity. Thus, emissivity can be less than one, but it is assumed to be constant across the waveband. Any significant deviation from a constant emissivity will introduce error. However, because of its insensitivity to translucent regions, the derivative method is regarded as the preferred calibration method for the pyrometer. This conclusion is further supported by the field test data described in **Chapter 6**.

CHAPTER 6

FIELD TESTING OF THE SENSOR

6.1. Experiment Setup

A field test experiment was devised to measure actual hydrocarbon flame data in order to validate the calibration of the pyrometer. Both the pyrometer and the SP-100 spectroradiometer were boresighted to simultaneously measure the same flame event. The data calculated from both sensors was compared as a final validation of the proposed pyrometer calibration method. The setup for this experiment is shown in **Figure 6.1**.

Figure 6.1 Experimental field test setup.

Hydrocarbon fuels cover a wide range of burn temperatures. Therefore, to test the pyrometer's effectiveness, flame measurements were taken using both a clean burning fuel and a soot-rich fuel. It is expected that, though cooler in temperature, soot-rich

flames will naturally perform better because of their near uniform high soot density [**54**]. Cleaner burning fuels present of more challenging test case. Though cleaner fuels will burn hotter, their low soot production leads to portions of the flame appearing translucent. As has been previously discussed, this translucence allows the background to become visible which can cause miscalculations in the flame temperature.

6.2. Background Removal and Correcting for Flame Translucence

In the previous chapter, two separate algorithms were presented by which flame temperatures could be calculated. However, before either can be evaluated, a method is needed whereby the image of the flame can be separated from the rest of the scene. If no background removal process exists, then either temperature calculation algorithm will blindly predict the "temperature" of the entire scene. An example of this improper temperature calculation is shown below in **Figure 6.2**. In the following section, a pre-processing algorithm is presented whereby the flame is located within the scene and all other pixels are zeroed out.

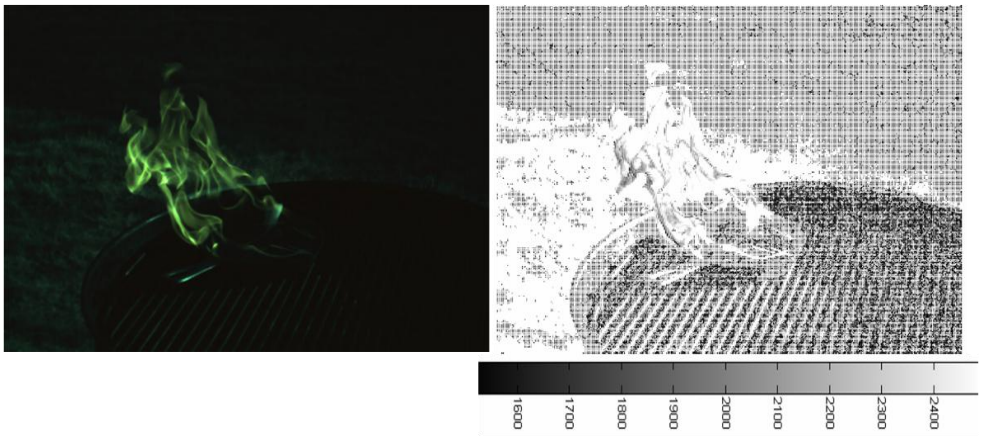

Figure 6.2 Grayscale image calculated by camera (left), unfiltered temperature calculation using derivative method

6.2.1. Pixel Thresholding

The first step, simply enough, is to filter out those pixels whose values are either too low, or two high. It is important to repeat that the dark noise for the camera has been measured to be between 10 to 16 counts, depending on the color channel. The dark noise measurements are first subtracted from the sensor's raw RGB image. The lower threshold value is hardwired at 22 counts. Therefore, as a minimum requirement, any given pixel in the sensor's raw RGB must have a value of 32 counts before the dark noise values are subtracted. Consequently, this lower limit of the threshold filter translates into requirement that any pixel must have an approximate SNR value of 2 in order to pass through this filter. The maximum value of the threshold filter is set to 250 in order to avoid operating on any saturated pixels. The threshold filtering is performed on each of the three color channels of each pixel independently. If any one of the three color values fails the threshold test, then that pixel is zeroed out.

6.2.2. Temperature Thresholding

The RGB values of pixels that satisfy the threshold filtering are then operated on by the temperature calculation algorithm which produces a 2D temperature image. Though two temperature calculation algorithms have been presented, the following process is utilized regardless of which temperature calculation algorithm is employed. A process must now be developed which is capable of accounting for any remaining pixels that correspond to non-flame portions of the scene. To do this, the temperature calculation algorithm itself is employed. The term temperature calculation algorithm is left ambiguous to indicate that this step is applicable to both the ratio and derivative methods.

In the visible portion of the spectrum, blackbody radiators occupy a unique portion of the total color space. Note that regardless of which temperature calculation algorithm is employed, both seek to define the specific spectral radiance distribution (i.e., the color space) occupied by a blackbody radiator at a given temperature. Consequently, when the temperature calculation algorithm is applied to a non-blackbody portion of the scene, the resulting "temperature" is nonsensical for a hydrocarbon flame as it will fall outside the theoretical range of possible temperature. Pixels with calculated temperatures outside this acceptable range are thus filtered out. Therefore this approach allows the flame to be identified within the scene and its temperature to be calculated without including any *a priori* knowledge of the type of hydrocarbon fuel. The only stipulation is that the flame radiate with a greybody spectral profile. The acceptable temperature range for a hydrocarbon flame is approximately 1070 K to 2720 K. The upper limit of 2720 K may in fact be too conservative; however the possibility of increasing this limit will be reserved for future research.

6.2.3. Removing Translucent Flame Regions

A third and final filter is required to account for portions of the scene where the flame is translucent. This is primarily a concern for cleaner burning flames, as opposed to soot-rich flames with a high soot output. These areas are statistically significant and must be address to prevent the temperature histogram from being skewed. For these translucent regions of the flame, the background can be observed through the flame. The values generated by the background visibility effectively functions as a DC offset to the count values for each color channel.

Referring back to the two temperature calculation algorithms, it is easy to see that the introduction of a DC offset will result in an improper calculation of the flame temperature in these regions when using the ratio method. The derivative method has been shown to be less sensitive to these background effects. However, there is a point where the light from the background will overwhelm the radiation emitted from the flame. Thus, translucence will still be considered for both algorithms. Currently, a method will be presented for identifying and removing these translucent regions. It is believed that future experimentation could provide a method whereby the background values could be determined. Such a technique would allow the background to be subtracted in order to recover the flame temperature for these regions.

From a review of the temperature calculation algorithms, it can be seen that the DC offset values introduced by the background will cause the calculated flame temperature to be higher than it actually is. This temperature shift presents a method whereby the translucent regions can be identified. To do this, pixels that have a resulting flame temperature between 2720 K and 4000 K are identified. These will be referred to as the high-end pixel group, which will be represented by P_h. These pixels are clearly outside the expected flame temperature range, but there is a high statistical probability that the temperature calculated for the translucent regions will fall within this range.

Translucent portions of the flame typically occur at the flame edges, where the carbon soot particles are beginning to cool. Thus, if the flame has multiple translucent areas, then scene background at one end of the flame will differ from the opposite end of the flame. Conversely, the presence of few translucent regions will maintain a degree of uniformity in the background. For this reason, the standard deviation of the high-end pixel group is a good indicator for the degree of flame translucence.

To filter out the translucent regions of the flame, a new temperature range is defined. As with the temperature threshold filter, the lower temperature range is still set at 1070 K; however, the upper limit is now defined as mean(P_h)-3*Standard Deviation(P_h). An example of this background removal process is presented below in **Figure 6.3 (left),** as well as the resulting imagery when the translucence removal filter is applied as in **Figure 6.3 (right)**. Histograms for both data sets are also presented. Note that this imagery data is the same as that presented in **Figure 6.2 (right)**, except that now the background removal algorithm has been applied. For the purposes of this illustration, the derivative temperature calculation algorithm was employed. However, the approach is the same for the ratio temperature calculation algorithm.

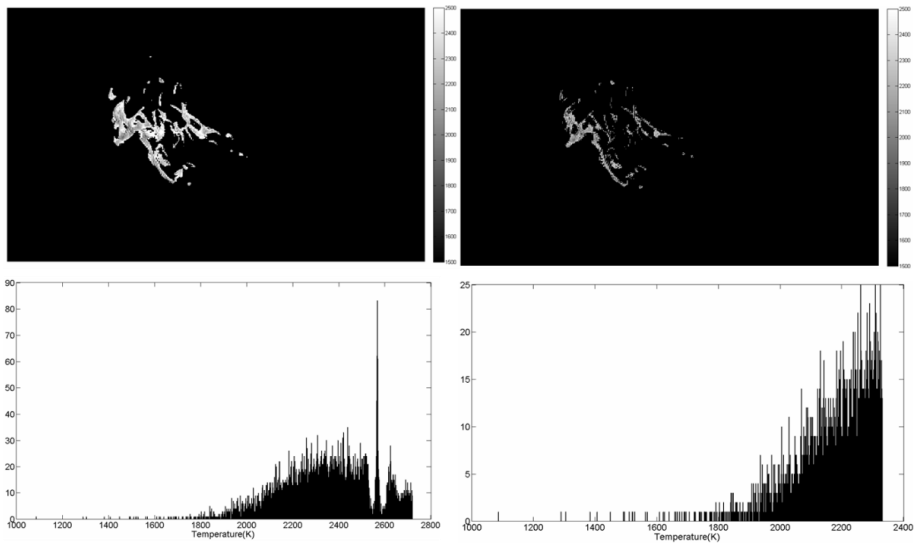

Figure 6.3 Output of temperature filter (upper left) and temperature histogram of image (lower left), versus output of translucence removal filter (upper right) and temperature histogram of image (lower right)

This approach treats the translucent portions of the flame as statistical outliers of the high pixel region. Pixels that pass this third and final filter are presented as the

calculated flame temperature of the scene. The flame temperature then can be presented on a pixel by pixel basis. Pixels that are rejected by any one of the above mentioned filters are zeroed out. Note that, as with the temperature calculation algorithm, the spatial resolution of the background removal algorithm is limited only by the resolution of the imaging sensor hardware.

It is envisioned camera the proposed sensor should function as a network of cameras monitoring a large area [**55**]. Therefore, it is anticipated that the temperature calculation algorithms as well as the filtering algorithms will not be implemented onboard the camera. Though smart cameras with onboard processing capabilities are an emerging technology, the risk of hardware loss due to flame damage does not make them a feasible option. For a deployable camera network to be a viable approach to flame detection, costs must be kept low. For this reason, it is envisioned that sensor data will be transmitted to a central hub for processing. This approach will be able to take advantage of pre-existing video distribution networks as a mosaic video is being transmitted over data lines [**56**,**57**,**58**,**59**]. This is significant because mosaic video requires the same amount of bandwidth as monochrome imagers, making the sensor well suited as upgrade hardware to existing infrastructure such as security camera systems.

6.3. Field Test Experiment Results

Once the background subtraction algorithm had been developed, a set of field test flame measurements was taken to evaluate the pyrometers performance. To do this, both the pyrometer and the SP-100 were boresighted to collect flame measurements simultaneously, much as they were during the initial calibration method described in **Chapter 5**. Two hydrocarbon fuels were poured into a pan approximately five feet away

from the sensor pair. The fuel was then ignited and both sensors measured the burn simultaneously. For this experiment, gasoline and isopropyl alcohol fires were measured by both sensors simultaneously. The gasoline flame serves as the soot-rich example while the isopropyl alcohol serves as the clean burning fuel [**60**,**61**]. Since isopropyl alcohol flames are clean burning, it is anticipated that they are more prone to have a high number of translucent regions. For this reason, this fuel was tested both in the daytime and at night.

An initial analysis of the field test data is presented below in **Table 6.1**. In-depth interpretation of the field test results is provided later on in this chapter. At first glance, the statistical results presented in **Table 6.1** indicate that both the derivative and ratio algorithms perform equally well. Furthermore, the ratio method appears to deliver a higher degree of accuracy than the derivative method for the daytime isopropyl flame. However, it is believed that this data cannot be taken at face value due to the influence of translucent regions on the calculated flame temperature. However, this data is presented first to help illustrate the difficulty in processing flame temperature images.

Table 6.1 Field Test Temperature Measurements Results

Sensor	SP-100		Derivative Method		Ratio Method	
Data Type	Temperature (K)	Standard Deviation (K)	Temperature (K)	Standard Deviation (K)	Temperature (K)	Standard Deviation (K)
Gasoline	1706	55	1764	187	1752	192
Isopropyl Daytime	1902	54	2151	149	2042	143
Isopropyl Night	1899	36	1850	124	1829	126

The SP-100 spectroradiometer has a 1.8^{o} full FOV. Because the FOV is so narrow, the sensor was aimed directly into the fuel pan to avoid translucent areas. By contrast, the imaging pyrometer has an approximately 55^{o} full FOV, and was positioned such that the whole fire could be seen. As a result, low emissivity areas near the edges of the flame are included in the pyrometer's temperature average. It is believed that these areas result in an over predicted average for both algorithms. Additionally, the analysis of the data revealed the pixel filtering algorithm (described in the previous chapter) zeroed out considerably more pixels when using the ratio method as compared to the derivative method. Therefore, while the averages of both methods appear equal, the temperature image reported by the derivative method is far denser than that of the ratio method. To help further explain these results, a more rigorous statistical analysis is presented below.

The algorithm used to calculate the blackbody temperature is the same as the one used to perform the sensor calibration described in **Section 5.2**. Though both measurements were collected concurrently, the Pyrometer recorded at a rate of approximately 6 Hz where as the SP-100 recorded at a rate of approximately 0.1 Hz. Because of this, the SP-100 was allowed to collect data during the entire burn event, where as the Pyrometer collected 100 frames at the beginning of the burn event and then a second set of 100 frames at the end of the SP-100's record times. As a result, the measurements taken at the beginning of the burn time measured hotter than those at the end when the fuel was beginning to run low. Sample radiance measurements from the SP-100 for the gasoline flame are given below in **Figure 6.4**. **Figure 6.5**, shown below, illustrates the temperatures calculated from the SP-100 measurements are shown in order to reflect the downward trend of the flame temperature over time.

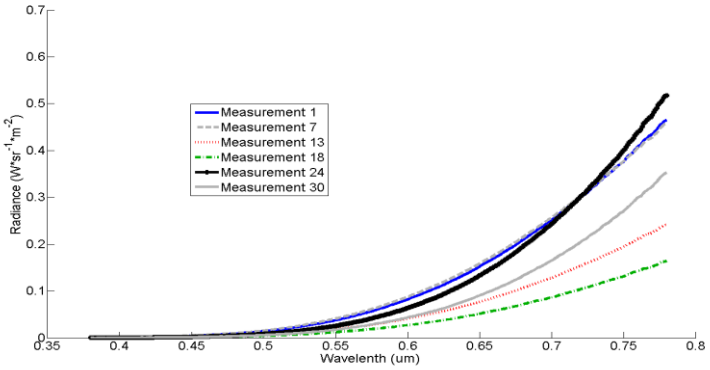

Figure 6.4 Radiance measurements of gasoline flame

The blackbody temperatures measured from the data collected by the SP-100 are shown below in **Figure 6.6** as a side-by-side comparison in order to validate the performance of the pyrometer.

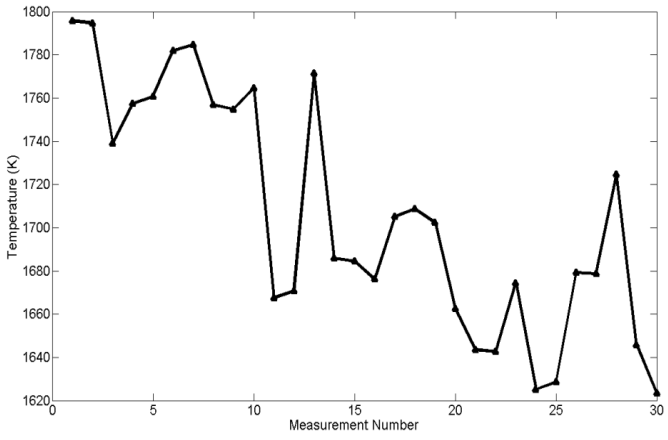

Figure 6.5 SP-100 calculated flame temperature versus time for gasoline flame

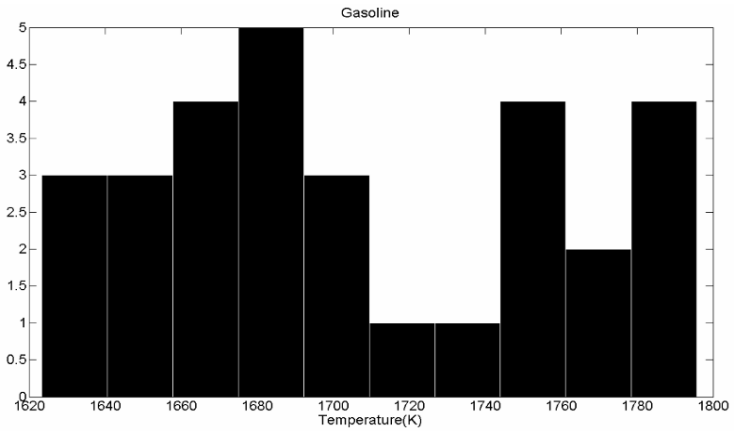

Figure 6.6 SP-100 blackbody temperature measurement histogram for gasoline flame

Figure 6.7 through **Figure 6.8**, shown below, present the associated flame temperatures calculated from the imaging pyrometer and the SP-100 for a nighttime gasoline flame event. Because the SP-100 is non-imaging sensor, a histogram representation of the data collected by both sensors allows for a side by side comparison of the data from both imaging pyrometer and the SP-100. Therefore, it is now possible to compare the data in **Figure 6.6** to that presented in **Figure 6.7** through **Figure 6.8**.

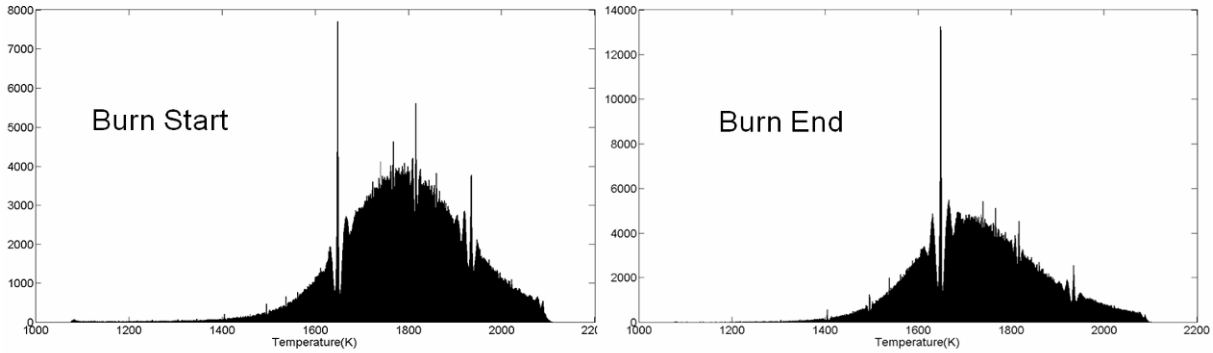

Figure 6.7 Imaging pyrometer gasoline flame temperature calculation histogram (derivative method)

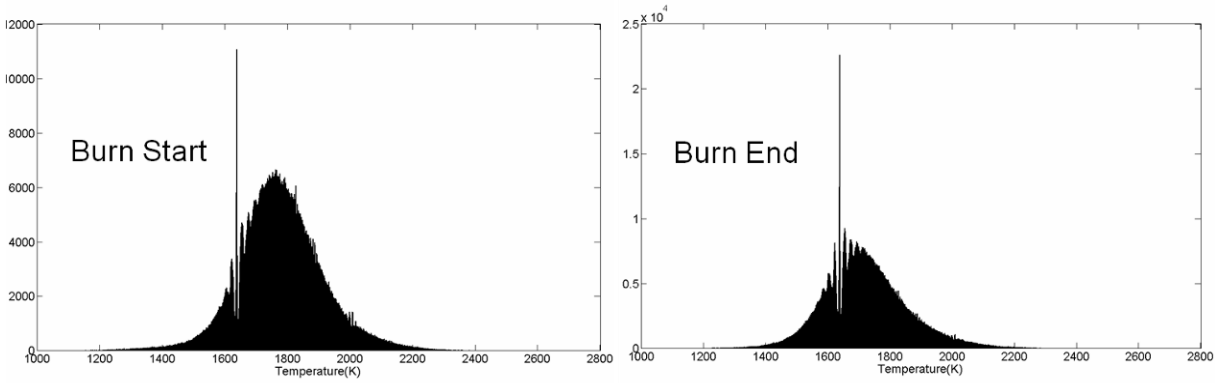

Figure 6.8 Imaging pyrometer gasoline flame temperature calculation histogram (ratio method)

Sample radiance measurements from the SP-100 for the gasoline flame are given below in **Figure 6.9**. Isopropyl produces a clean burning flame when compared to a gasoline flame which results a high number of translucent regions. For this reason, both daytime and nighttime measurements were taken to determine how this translucent affects the measured flame temperature. **Figure 6.10**, shown below, illustrates the temperatures calculated from the SP-100 measurements are shown in order to reflect the steady trend of the flame temperature over time.

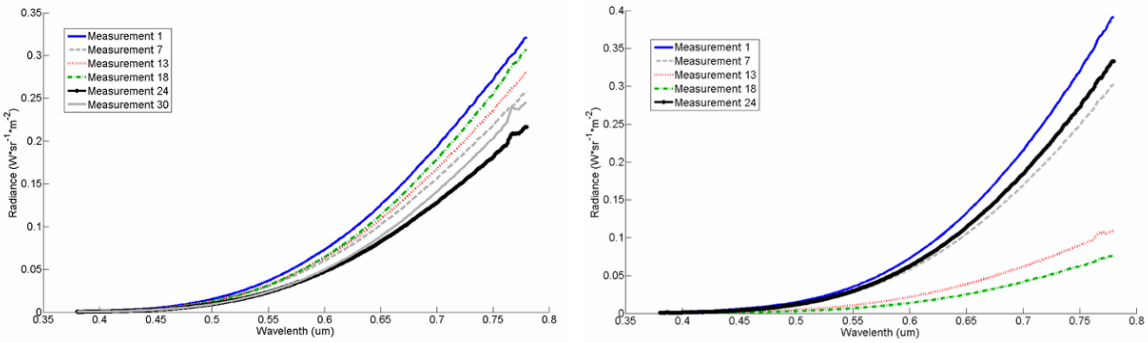

Figure 6.9 Radiance measurements of isopropyl flame night time (left) and daytime (right)

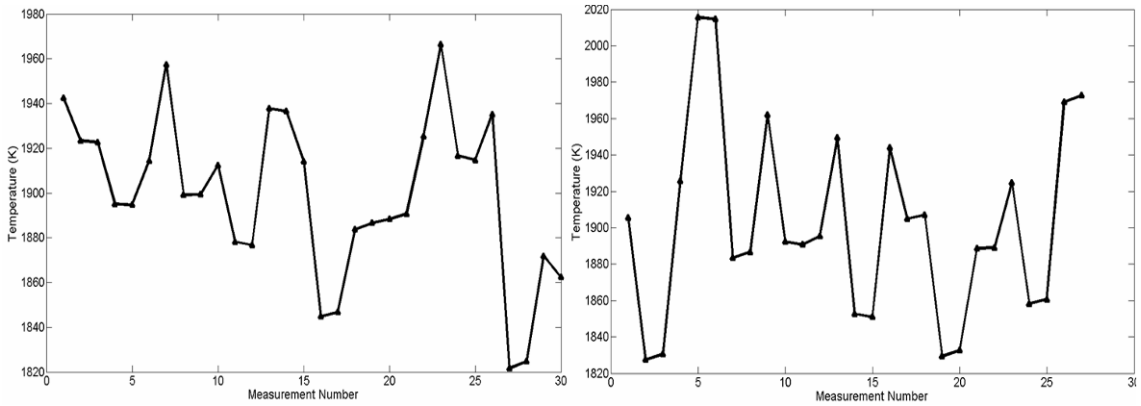

Figure 6.10 SP-100 calculated flame temperature versus time for isopropyl flame night time (left) and daytime (right)

Figure 6.11 and **Figure 6.12**, shown below, present the associated flame temperatures calculated from the imaging pyrometer and the SP-100 for both daytime and nighttime isopropyl flame events. Because the SP-100 is non-imaging sensor, a histogram representation of the data collected by both sensors allows for a side-by-side comparison in order to validate the performance of the pyrometer.

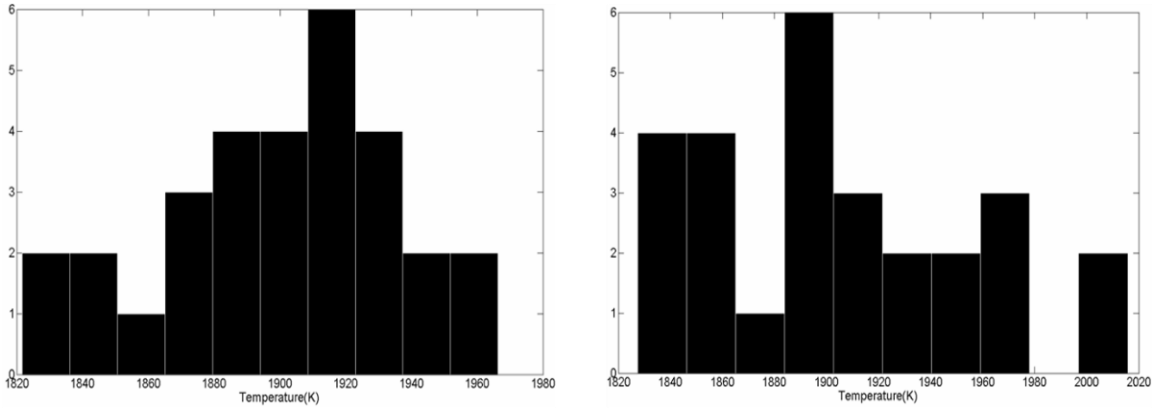

Figure 6.11 SP-100 isopropyl flame temperature calculation, night time (left) vs. daytime (right)

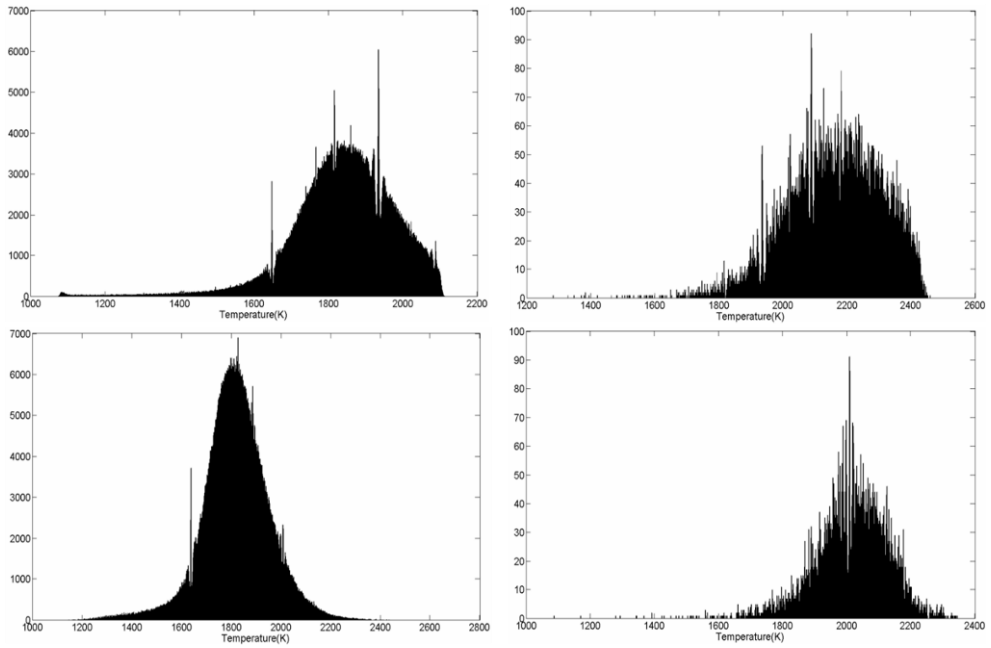

Figure 6.12 Imaging pyrometer isopropyl flame temperature calculation histogram derivative method-night time (upper left), derivative method-day time (upper right), ratio method-night time (lower left), ratio method-day time (lower right)

CHAPTER 7

CONCLUSIONS AND FUTURE RESEARCH

7.1. Project Discussion

This research effort has presented an argument for the design and calibration of an imaging pyrometer for use with hydrocarbon fuels. Initial studies on the burn profile of hydrocarbon flames lead to the conclusion that such a sensor could be based on a pixilated array with a responsivity in the visible waveband. With the proliferation of high resolution color CMOS and CCD arrays, there is the potential to create a low cost pyrometer sensor based on this technology.

The core of this project has focused on the development of a calibration algorithm capable of determining the temperature of a flame within the FOV on a pixel-by-pixel basis. Through experimentation, two candidate algorithms were developed that monitor how the color space of a blackbody radiator changes as a function of temperature. The first algorithm uses a simple ratio representation of the sensor's three color channels. The second algorithm relates the flame temperature to the power distribution across the three color channels.

Through an investigation of these algorithms, it has been determined that both methods are immune to flame emissivity. Here, emissivity can be less than one, but it is assumed to be constant across the waveband; resulting in a greybody. If there is a significant divergence from a constant emissivity, error will be introduced. Nevertheless, given that carbon soot is the primary radiator in the visible region for these types of flames, a uniform emissivity is anticipated.

Both algorithms were tested and evaluated in the laboratory and with field environments using flame data from both clean and soot-rich burning fuels. Both algorithms have proven effective for those portions with high soot production. However, for those flame regions where there is high translucence, as often present in clean burning fuels, the derivative algorithm delivers superior performance over the simple ratio algorithm. The reason for this is based on the nature of the algorithms themselves. As described in the previous chapters, for translucent regions, the background becomes visible and acts as a DC offset for the count values for the three color channels. For the ratio method, the introduction of a DC offset will cause a skew in the temperature prediction.

For the polynomial derivative temperature calculation algorithm, the count values for the three color channels are fit to a second order polynomial and the peak of the polynomial is related to temperature. It was readily apparent that the derivative of a DC component was zero. This of course assumes that the background is dark and introduces a near uniform DC offset. Additionally, a greybody's spectral emission profile was assumed for the curve fit. This insensitivity to translucent regions lead to the derivative method being chosen as the preferred calibration method for the pyrometer.

7.2. Future Research

One of the primary areas for future research will be the implementation of advanced DeBayer algorithms. The scientific camera presented in the paper uses an internal, onboard bilinear interpolation DeBayer algorithm. Bilinear interpolation, while efficient, is subject to "Bayer Artifacts" where there are errors in color registration. This effect is most pronounced at edge points with high contrast. Because color is a composite

of the three RGB intensities, a misregistration in reported color directly results in temperature calculation error. For future research, effort will be made to identify more robust DeBayer algorithms to improve the accuracy of the reported flame temperature [**62**,**63**].

Future research will be centered around the development of a more robust background correction algorithm rather than the simple background removal process currently employed. Such an algorithm will allow for the dynamic identification of a flame event in order to more accurately calculate the flame temperature. A dynamic background correction algorithm will allow for the deployment of this sensor into the field. Such advancements will allow for rapid sensor setup and thus lower the cost of utilizing the proposed technology.

Additional research will also focus on identifying non-flame light sources that could serve to skew the temperature within the scene. Of specific interest are solar reflections off objects within the scene. The mitigation of the effects of non-flame sources will also help to expedite the setup process of the sensor for field test measurements. It is anticipated that if the sensor is capable of operating without putting restrictions on the scene. This will prove a more useful tool for flame research.

REFERENCES

[**1**] Arias, L., Torres, S., Sbarbaro, D., Farias, O. (2008). Photodiode-based sensor for flame sensing and combustion-process monitoring. *Appl. Opt.* **47**(29)**:** 5541-5549.

[**2**] Kennett, S.R., Lambrineas, P., Suendermann, B., Woodward, R.L. (1991). *A Fire Risk Assessment Methodology For Naval Vessels*. St. Petersburg, Florida.

[**3**] Sorathia, U., Gracik, T., Ness, J., Durkin, A., Williams, F., Hunstad, M., and Berry, F. (2003) Evaluation of intumescent coatings for hipboard fire protection, *Journal of Fire Sciences, 21*(6): 28.

[**4**] Ohlemiller, T., Clearly, T., Brown, J., Shields, J. (1993). Assessing the flammability of composite materials. *Journal of Fire Sciences* **11:** 12.

[**5**] Brown, J., Braun, E., Twilley, W. (1988). *Cone Calorimeter Evaluation of the Flammability of Composite Materials*. U.S. Department of Commerce.

[**6**] Sun, L., Zhou, X., Mahalingam, S., Weise, D.R. (2006). Comparison of burning characteristics of live and dead chaparral fuels. *Combustion and Flame* **144**(1-2)**:** 349-359.

[**7**] Riggan, P.J., Hoffman, J.W., Brass, J.A. (2000). Estimating fire properties by remote sensing. *Aerospace Conference Proceedings, 2000 IEEE* **3:** 173-179 vol.173.

[**8**] Loyd, R. (1994). *Machine Vision Fire Detection Technology*. U.S. Army Armament, Munitions and Chemical Command, Safety Office**:** 20

[**9**] Schultze, T., Kempka, T., Willms, I., (2006). Audio-video fire-detection of open fires. *Fire Safety Journal* **41**(4)**:** 311-314.

[**10**] Toreyin, B.U., Dedeoglu, Y., Cetin, A.E. (2005). Flame detection in video using hidden Markov models. *Image Processing, 2005. ICIP 2005. IEEE International Conference on* **2:** II-1230-1233.

[**11**] She, X., Huang, F. (2009). Flame edge detection based on C-V active contour model. *Artificial Intelligence and Computational Intelligence, 2009. AICI '09. International Conference on* **2:** 413-417.

[**12**] Lin, S., Zhe, C. (2009). The flame detection and background interference filtering algorithm based on video images. *Computer Science and Information Engineering, 2009 WRI World Congress on* **6:** 559-563.

[**13**] Çelik, T., Demirel, H. (2009). Fire detection in video sequences using a generic color model. *Fire Safety Journal* **44**(2)**:** 147-158

[**14**] Li, D. (2006). Thermal Image Analysis Using Calibrated Video Imaging. **Doctor of Philosophy**: 126.

[**15**] Shaw, B. (2005). *Dual-Band Video Camera*. Rochester: Center for Imaging Science Rochester Institute of Technology.

[**16**] Lou, C., Zhou, H.C., Yu, P.F., Jiang, Z.W. (2007). Measurements of the flame emissivity and radiative properties of particulate medium in pulverized-coal-fired boiler furnaces by image processing of visible radiation. *Proceedings of the Combustion Institute* **31**(2)**:** 2771-2778.

[**17**] Pluchino, A.B., Goldberg, S.S., Dowling, J.M., Randall, C.M. (1980). Refractive-index measurements of single micron-sized carbon particles. *Appl. Opt.* **19**(19)**:** 3370-3372.

[**18**] Batten, C.E. (1985). Spectral optical constants of soots from polarized angular reflectance measurements. *Appl. Opt.* **24**(8)**:** 1193-1199.

[**19**] Block, B., Hentschel, W., Ertmer, W. (1998). Pyrometric determination of temperature in rich flames and wavelength dependence of their emissivity. *Combustion and Flame* **114**(3-4)**:** 359-369.

[**20**] Plimpton, J.C. (Northfield, NH), Minott, G.L. (Wilton, NH) (1994). UV/IR fire detector with dual wavelength sensing IR channel. (US 5311167).

[**21**] Keyvan, S., Rossow, R., Romero, C., Li, X. (2004). Comparison between visible and near-IR flame spectra from natural gas-fired furnace for blackbody temperature measurements. *Fuel* **83**(9)**:** 1175-1181.

[**22**] Owrutsky, J.C., Steinhurst, D.A., Minor, C.P., Rose-Pehrsson, S.L., Williams, F.W., Gottuk, D.T. (2006). Long wavelength video detection of fire in ship compartments. *Fire Safety Journal* **41**(4)**:** 315-320.

[**23**] Raj, P.K. (2007). LNG pool fire spectral data and calculation of emissive power. *Journal of Hazardous Materials* **142**(3)**:** 720-729.

[**24**] Griffin, M.K., Burke, H.K., Kerekes, J.P. (2004). Understanding radiative transfer in the midwave infrared: a precursor to full-spectrum atmospheric compensation. *SPIE* **5425:** 348-356.

[**25**] Kaplinsky, M.B. (South Orange, NJ), Kosonocky, W.F., (Skillman, NJ), Mccaffrey, N.J. (Clifton, NJ) (1998). Multi-wavelength imaging pyrometer. (US 5822222).

[**26**] Gang, L., Yong, Y. (2006). Temperature profiling of pulverized coal flames using multicolor pyrometric and digital imaging techniques. *Instrumentation and Measurement, IEEE Transactions on* **55**(4)**:** 1303-1308.

[**27**] Seitz, P. (Urdorf, CH) (2004). Imaging pyrometer. (US 6758595).

[**28**] Abe, H. (2004). Device technologies for high quality and smaller pixel in CCD and CMOS image sensors. *Electron Devices Meeting, 2004. IEDM Technical Digest. IEEE International***:** 989-992.

[**29**] Miller, H. (1996). Improved color filter process for CCD and CMOS imagers. *Advanced Semiconductor Manufacturing Conference and Workshop, 1996. ASMC 96 Proceedings. IEEE/SEMI 1996***:** 192-195.

[**30**] Brown, L.G. (1992). A survey of image registration techniques. *ACM Comput. Surv.* **24**(4)**:** 325-376.

[**31**] Vaulina, O.S., Nefedov, A.P., Petrov, O.F., Samarian, A.A., Chernyschev, A.W. (1998). Temperature measurements of optically non-gray particles in high-temperature dusty media. *Combustion and Flame* **115**(3)**:** 364-371.

[**32**] Fu, T., Yang, Z., Wang, L., Cheng, X., Zhong, M., Shi, C. (2010a). Measurement performance of an optical CCD-based pyrometer system. *Optics & Laser Technology* **42**(4)**:** 586-593.

[**33**] Huston, J.T. (Sugar Grove, OH), Youssef, Simon F. (Lancaster, OH) (2007). Two-color flame imaging pyrometer. (US 20070177650).

[**34**] Hou, X., Zhao, W., Yao, B. (2007). Accuracy of two-color pyrometry using color high-speed cameras for measurement of luminous flames. *SPIE*. pp 627918-627919.

[**35**] Jiang, Z.W., Luo, Z.X., Zhou, H.C. (2009). A simple measurement method of temperature and emissivity of coal-fired flames from visible radiation image and its application in a CFB boiler furnace. *Fuel* **88**(6)**:** 980-987.

[**36**] Jenkins, T.P., Hanson, R.K. (2001). Soot pyrometry using modulated absorption/emission. *Combustion and Flame* **126**(3)**:** 1669-1679.

[**37**] Hottel, H.C., Broughton, F.P. (1932). Determination of True Temperature and Total Radiation from Luminous Gas Flames. *Industrial & Engineering Chemistry Analytical Edition* **4**(2)**:** 166-175.

[**38**] Lindberg, J.D., Douglass, R.E., Garvey, D.M. (1993). Carbon and the optical properties of atmospheric dust. *Appl. Opt.* **32**(30)**:** 6077-6081.

[**39**] Stull, V.R., Plass, G.N. (1960). Emissivity of dispersed carbon particles. *J. Opt. Soc. Am.* **50**(2)**:** 121-125.

[**40**] Murphy, J.J., Shaddix, C.R. (2005). Influence of scattering and probe-volume heterogeneity on soot measurements using optical pyrometry. *Combustion and Flame* **143**(1-2)**:** 1-10.

[**41**] Mikron Blackbody Radiation Calibration Sources (www.mikroninfrared.com)

[**42**] Perry, R.J. (1999). Analysis and characterization of the spectral response of CMOS based integrated circuit (IC) photodetectors. *University/Government/Industry Microelectronics Symposium, 1999. Proceedings of the Thirteenth Biennial***:** 170-175.

[**43**] Tairan, F., Xiaofang, C., Congling, S., Maohua, Z., Tiemin, L., Xiaobing, Z. (2006). The set-up of a vision pyrometer. *Measurement Science and Technology* **17**(4)**:** 659.

[**44**] McCluney, R. (1994). Introduction to Radiometry and Photometry**:** 402.

[**45**] Siegel, R., Howell, J.R. (1971). Thermal Radiation Heat Transfer**:** 814.

[**46**] The Imaging Source - "FireWire Cameras - Spectral sensitivity and color formats"

[**47**] Fu, T., Zhao, H., Zeng, J., Wang, Z., Zhong, M., Shi, C. (2010). Improvements to the three-color optical CCD-based pyrometer system. *Appl. Opt.* **49**(31)**:** 5997-6005.

[**48**] Johnson, R. (West Brattleboro, VT) (1997). Optical filters for forming enhanced images. (5646781).

[**49**] Gage, H.P. (1933). Color Filters for Altering Color Temperature. Pyrometer Absorption and Daylite Glasses. *J. Opt. Soc. Am.* **23**(2)**:** 46-54.

[**50**] Nayar, S.K., Ben-Ezra, M. (2004). Motion-based motion deblurring. *Pattern Analysis and Machine Intelligence, IEEE Transactions on* **26**(6)**:** 689-698.

[**51**] Matlab Help Document (R2010a) (www.mathworks.com/help)

[**52**] Turner, L.R. (1966). Inverse of the Vandermonde Matrix with applications. (NASA TN D-3547)**:** 1-17.

[**53**] Williams, P.A., Rose, A.H., Wang, C.M. (1997). Rotating-polarizer polarimeter for accurate retardance measurement. *Appl. Opt.* **36**(25)**:** 6466-6472.

[**54**] Lee, C.B., Lee, W., Oh, K.C., Shin, H.D., Yoon, J.K. (2006). Sooting and non-sooting propylene diffusion flames with irradiation of laser light. *Combustion, Explosion, & Shock Waves* **42**(6)**:** 688-695.

[**55**] Ko, B.C., Cheong, K.H., Nam, J.Y. (2009). Fire detection based on vision sensor and support vector machines. *Fire Safety Journal* **44**(3)**:** 322-329.

[**56**] Bhuiyan, S.M.A., Khan, J.F., Attoh-Okine, N.O., Adhami, R.R. (2009). Study of bidimensional empirical mode decomposition method for various radial basis function surface interpolators. *Machine Learning and Applications, 2009. ICMLA '09. International Conference on***:** 18-24.

[**57**] Khan, J., Barner, K., Adhami, R. (2008). Feature point detection utilizing the empirical mode decomposition. EURASIP *Journal on Advances in Signal Processing*, **2008:** 3-15

[**58**] Xiang, X., GuoLin, L., XiaoWen, L., Chun, Z., ZhiHua,W., XinKaiChen, HsiaoWeiSi. (2004). A new high quality image compression method for digital image sensors with Bayer color filter arrays. *Biomedical Circuits and Systems, 2004 IEEE International Workshop on***:** S3/3-13-16.

[**59**] Sang-Yong, L., Ortega, A. (2001). A novel approach of image compression in digital cameras with a Bayer color filter array. *Image Processing, 2001. Proceedings. 2001 International Conference on* **3:** 482-485 vol.483.

[**60**] Bruce, C.W., Stromberg, T.F., Gurton, K.P., Mozer, J.B. (1991). Trans-spectral absorption and scattering of electromagnetic radiation by diesel soot. *Appl. Opt.* **30**(12)**:** 1537-1546.

[**61**] Huang, C., Wie, L., Yang, B., Wang, J., Li, Y., Sheng, L., Zhang, Y., Qi, F. (2006). Lean premixed gasoline/oxygen flame studied with tunable synchrotron vacuum UV photoionization. *Energy & Fuels* 20(4): 1505-1513.

[**62**] Dubois, E. (2006). Filter design for adaptive frequency-domain Bayer demosaicking. *Image Processing, 2006 IEEE International Conference on***:** 2705-2708.

[**63**] Condat, L. (2010). A simple, fast and efficient approach to denoisaicking: Joint demosaicking and denoising. *Image Processing (ICIP), 2010 17th IEEE International Conference on***:** 905-908.

VITA

Jonathan Braun Hanks received a Bachelor of Science degree in Engineering from the University of Alabama in Huntsville (UAH) in May of 2006. In that same month he joined the engineering team at Polaris Sensor Technologies where he is currently employed as an Electro-Optical Engineer. He returned to UAH in the Fall of 2006 to begin work on his Master of Science in Engineering. He will obtain this degree in May of 2011.